Materials Today Bio 31 (2025) 101528

Contents lists available at ScienceDirect

Materials Today Bio

journal homepage: www.journals.elsevier.com/materials-today-bio

Physically engineered extracellular vesicles targeted delivering miR-21-5p to promote renoprotection after renal ischemia-reperfusion injury

Di Wu [a,1], Wenjie Ma [a,1], Liucheng Wang [b,1], Chengcheng Long [a], Silin Chen [a], Jingyu Liu [a], Yiguan Qian [a], Jun Zhao [a], Changcheng Zhou [a,*], Ruipeng Jia [a,**]

[a] Department of Urology, Nanjing First Hospital, Nanjing Medical University, Nanjing, 210006, China
[b] Department of Urology, Lianshui People's Hospital, Kangda College Affiliated to Nanjing Medical University, Jiang Su, 223400, China

ARTICLE INFO

Keywords:
Engineering
Extracellular vesicle
Neutrophil
Cell membrane
Renoprotection
miRNAs

ABSTRACT

Acute kidney injury (AKI) resulting from ischemia-reperfusion injury (IRI) is a common challenge in various clinical practices, yet effective therapies remain elusive. Endothelial injury plays a crucial role in the pathogenesis of renal IRI. Endothelial progenitor cells (EPCs) derived extracellular vesicles (EVs) hold promise as cell-free therapies for treating renal IRI; however, their efficacy is limited by low delivery efficiency. In this study, we developed neutrophils (NEs) membrane-modified EVs (N-EVs) by exploiting the natural properties of NEs to target damaged endothelium. N-EVs inherited the characteristic membrane proteins of NEs along with the biological functions of EPCs-EVs. Results from *in vitro* and *in vivo* experiments demonstrated that N-EVs significantly enhanced the targeting efficiency of EVs towards IRI kidneys via P-selectin glycoprotein ligand-1 (PSGL-1). Moreover, N-EVs effectively promoted the proliferation, migration, and tube-formation abilities of injured endothelial cells (ECs) and contributed to overall renal function improvement in IRI kidneys through targeted delivery of miR-21-5p. Additionally, N-EVs could restore damaged endothelial integrity, reduce cytokine release, and inhibit leukocyte infiltration, hence alleviating renal inflammation. In conclusion, our accessible engineering approach represents a promising strategy for treating renal IRI. Furthermore, this membrane hybrid modification can be tailored and optimized for broader applications in treating other diseases.

1. Introduction

Renal ischemia-reperfusion injury (IRI) refers to the aggravation caused by blood flow reperfusion following ischemia, which frequently occurs in clinical practice, such as renal transplantation, nephron-sparing surgery, severe trauma, and hemorrhagic shock [1–3]. Vascular injury plays a key role in the development of renal IRI and mediates the progression of chronic kidney disease (CKD) [4]. During IRI, injured endothelial cells (ECs) exacerbate renal hypoxia by disrupting endothelial integrity, recruiting inflammatory cells, and decreasing peritubular capillary density, which promotes increased injury and gradual progression to CKD [5].

Extracellular vesicles (EVs) are nanosized lipid-bilayer membrane vesicles containing proteins, nucleic acids, and lipids, serving as crucial mediators of intercellular communication [6,7]. Compared to conventional cell-based therapies, EVs offer exceptional biological properties, including low immunogenicity, high payload capacity, and available modification [8]. Notably, endothelial progenitor cell (EPCs)-derived EVs are widely demonstrated to exhibit promising therapeutic efficacy for ischemic diseases and facilitate renoprotection through miRNA delivery [9–12]. However, akin to other naturally secreted EVs, EPCs-derived EVs lack tissue-specific targeting capabilities, limiting their ultimate efficacy [13].

Neutrophils (NEs) are the most abundant circulating leukocytes and the first responders to activated endothelium. During renal IRI, NEs can adhere to the injured endothelium via interactions between increased adhesion molecules on ECs and corresponding receptors on NEs [14,15]. Notably, the binding of P-selectin glycoprotein ligand-1 (PSGL-1) (on NEs) and P-, E-selectin (on ECs) plays a key role in the early adhesion process [16]. Following endothelial adhesion, NEs migrate into renal parenchyma, triggering a cascade of inflammatory responses [17].

The natural targeting ability of NEs towards damaged endothelium

* Corresponding author. Department of Urology, Nanjing First Hospital, Nanjing Medical University, 68 Changle Road, Nanjing, 210006, China.
** Corresponding author. Department of Urology, Nanjing First Hospital, Nanjing Medical University, 68 Changle Road, Nanjing, 210006, China.
E-mail addresses: zhoucc@njmu.edu.cn (C. Zhou), urojiarp@njmu.edu.cn (R. Jia).
[1] These authors contributed equally to this work.

https://doi.org/10.1016/j.mtbio.2025.101528
Received 23 September 2024; Received in revised form 13 January 2025; Accepted 27 January 2025
Available online 30 January 2025

inspires an effective strategy for targeting damaged endothelium. Recent studies have demonstrated that NEs membrane-derived vesicles or NEs membrane-modified nanoparticles could specifically target the inflamed endothelium of the lung [18,19]. Since the endothelial targeting ability of NEs originates from several proteins on their membranes, NEs membrane-modified EVs may possess the targeting ability to the damaged kidney endothelium and thereby facilitate renoprotection.

In this study, we present a practical and effective approach for modifying EVs using NEs membranes, harnessing both the natural endothelial targeting capability of NEs and the therapeutic potential of EVs. Specifically, EPCs-derived EVs and NEs membrane vesicles (NMVs) were fused to generate NEs membrane-modified EVs (N-EVs). Following the comprehensive characterization of the physicochemical properties of N-EVs, the renal targeting and nephroprotective effects of N-EVs were investigated.

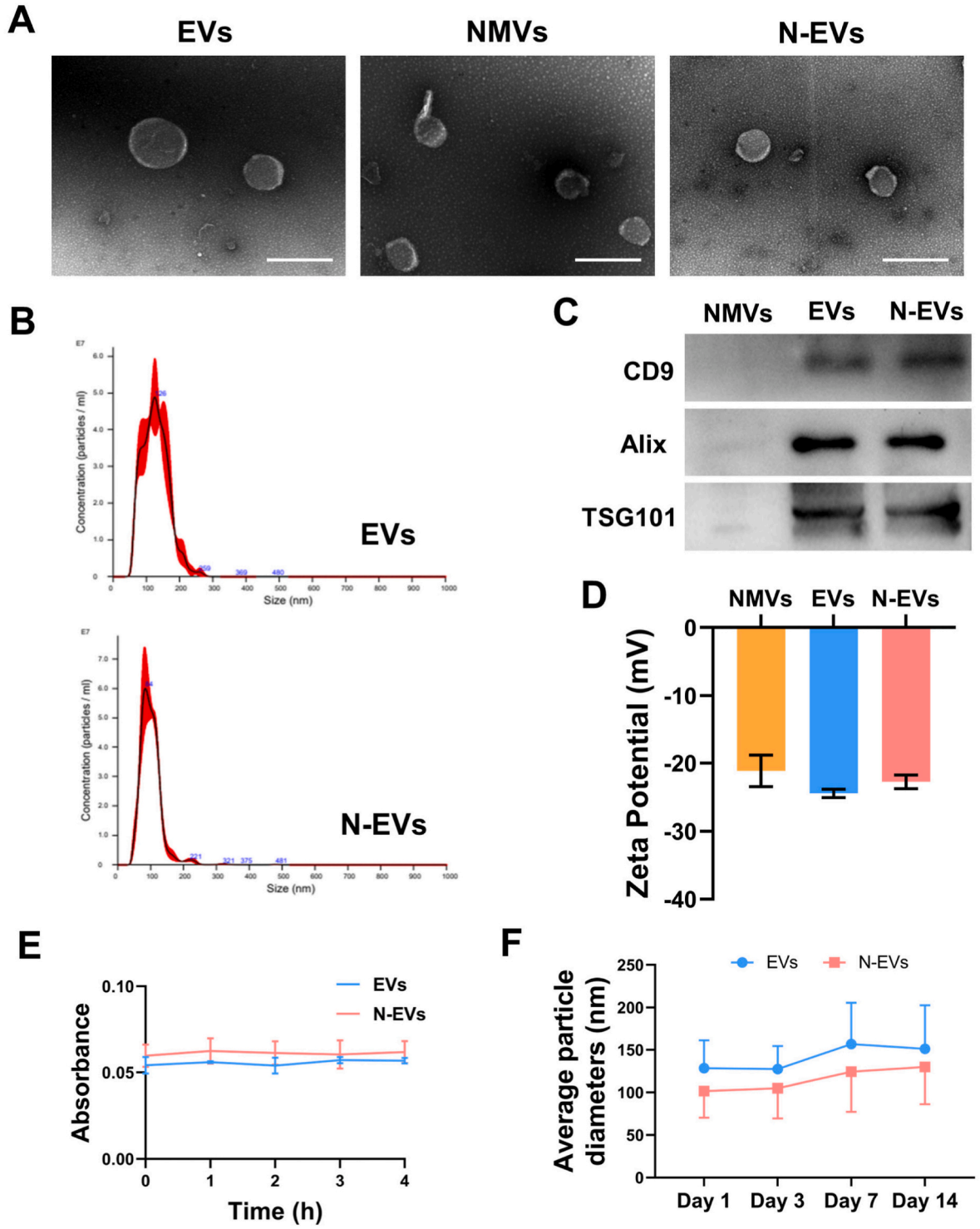

Fig. 1. Characterization of N-EVs. (A) TEM images of EVs, NMVs, and N-EVs. Scale bar = 200 nm. (B) NTA results of EVs and N-EVs. (C) WB assasys of CD9, Alix, and TSG101 in NMVs, EVs, and N-EVs. (D) The surface zeta potential results of EVs, NMVs, and N-EVs. (E) Colloid stability of EVs and N-EVs. (F) Detection of the average particle diameters of EVs and N-EVs at 4 °C within 14 days.

2. Results

2.1. Preparation and characterization of N-EVs

NEs constitute the predominant leukocyte population (40–75 %) in blood, while EPCs are typically derived from peripheral blood mononuclear cells (PBMCs) [20,21]. In this study, NEs and EPCs were both isolated from rat peripheral blood and characterized by flow cytometry and immunofluorescence staining. Flow cytometry determined that the extracted NEs highly expressed CD11b and RP-1 (Fig. S1A). Meanwhile, EPCs expressed CD34, CD133, CD31, and VEGFR-2, and were negative for CD14 and CD45 (Fig. S1C). Additionally, isolated EPCs could uptake Dil-Ac-LDL and bind FITC-UEA-1 (Fig. S1B). These results demonstrated the successful extraction of high-purity NEs and EPCs, consistent with previous studies [22,23].

EVs were obtained from the conditioned medium of EPCs using ultracentrifugation, while NMVs were generated from NEs via repeated freeze-thaw and extrusion. Subsequently, EVs and NMVs were fused to produce hybrid nanovesicles termed N-EVs via sonication and sequential extrusion techniques. TEM analysis demonstrated that EVs, NMVs, and N-EVs exhibited similar vesicle-like morphology (Fig. 1A). NTA revealed that the average particle diameters of EVs and N-EVs were 127.7 ± 39.0 nm and 100.1 ± 33.3 nm, respectively (Fig. 1B). Furthermore, N-EVs expressed exosome-associated markers including

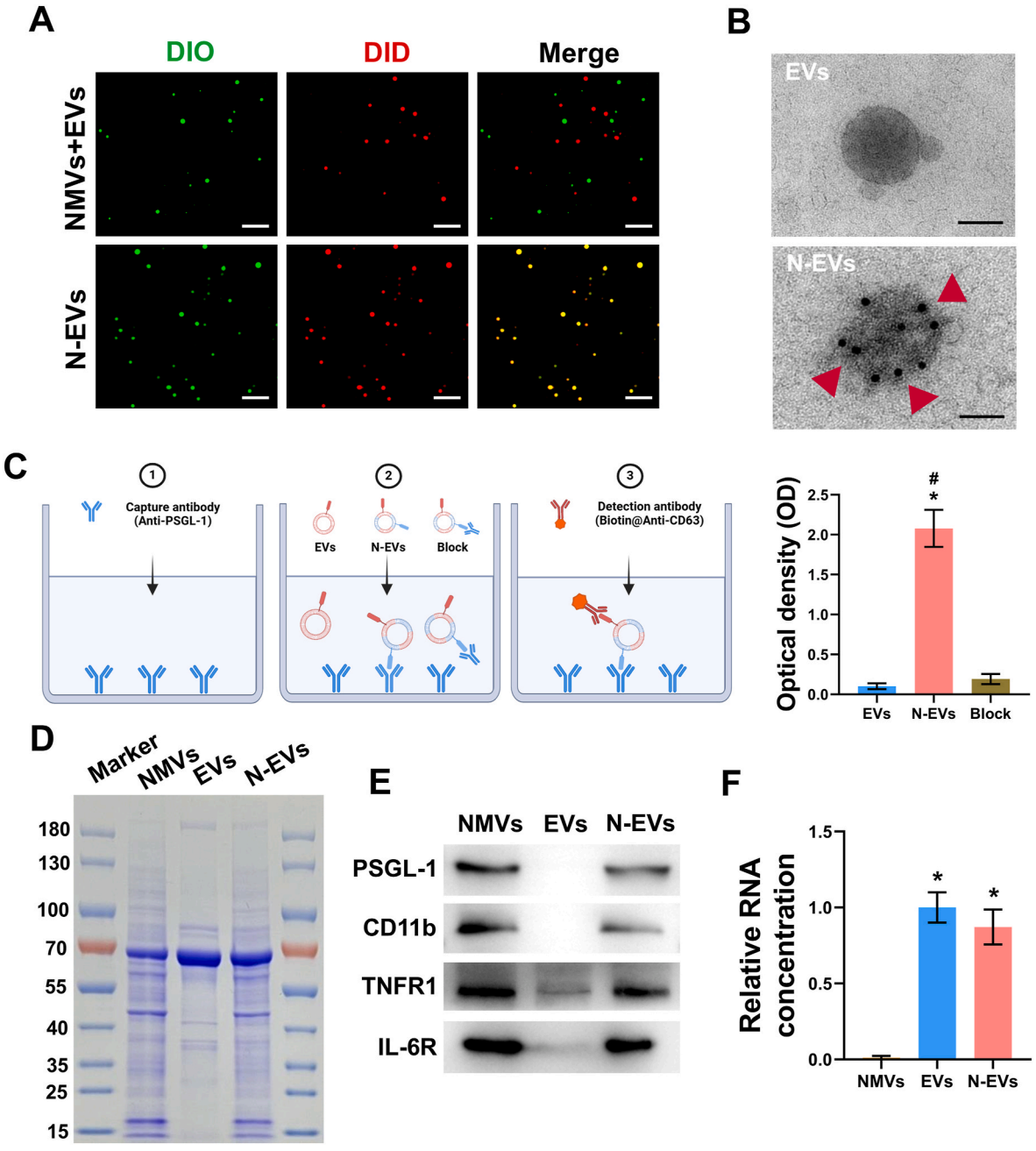

Fig. 2. Membrane fusion verification of N-EVs. (A) Immunofluorescence images of N-EVs or a mixture of EVs and NMVs without fusion. (DIO: NMVs; DID: EVs). Scale bar = 20 μm. (B) Immunogold-stained TEM images of EVs and N-EVs to detect PSGL-1 (red arrows, 10 nm gold nanoparticles). Scale bar = 50 nm. (C) Designed ELISA analysis for detection of PSGL-1 expression on N-EVs. Block, N-EVs blocked with anti-PSGL-1 antibody. *$P < 0.05$ vs. EVs; #$P < 0.05$ vs. Block. (D) The protein profiles of NMVs, EVs, and N-EVs on a Coomassie blue-stained SDS-PAGE gel. (E) Western blot analysis of PSGL-1, CD11b, TNFR1, and IL-6R in NMVs, EVs, and N-EVs. (F) Relative RNA concentration of NMVs, EVs, and N-EVs using a microplate reader. *$P < 0.05$ vs. NMVs.

CD9, Alix, and TSG101, instead NMVs rarely exhibit these hallmarks due to their synthetic nature (Fig. 1C). To comprehensively evaluate the colloidal, serum, and solution stability of N-EVs, we employed zeta potential analysis, absorbance assay, and a 14-day NTA. Although the zeta potential of N-EVs was slightly lower than that of EVs, this difference was not statistically significant (Fig. 1D). Moreover, EVs and N-EVs were suspended in 10 % human plasma, and no statistically significance changes in absorbance were observed within 4 h. Furthermore, the average particle diameters of EVs and N-EVs showed no significant difference after storage at 4 °C for 14 days. These findings suggested that N-EVs exhibit a comparable stability profile to that of EVs (Fig. 1E and F).

2.2. Confirmation of membrane fusion

To confirm whether the membrane fusion between EVs and NMVs was successfully conducted, we performed immunofluorescence, IEM, ELISA, and WB experiments. For immunofluorescence, NMVs were labeled with DIO and EVs with DID. There was no overlap area displayed between EVs and NMVs before extrusion. However, following the membrane fusion procedure, the fused N-EVs showed the colocalization of DID and DIO fluorescence (Fig. 2A). In the IEM images, the membrane of N-EVs exhibited multiple gold particles from PSGL-1 secondary antibody, instead these were absent on EVs membrane (Fig. 2B). In the modified ELISA assays, N-EVs could bind to the pre-coated capture antibody, while the vast majority of EVs and PSGL-1-blocked N-EVs were subsequently removed during the elution step. Additionally, CD63 was identified as a stable biomarker for EVs [24]. The results confirmed the expression of both CD63 (from EVs) and PSGL-1 (from NMVs) on the membrane of N-EVs (Fig. 2C; S2). SDS-PAGE gels were used to analyze whole protein extracts of NMVs, EVs, and N-EVs. After Coomassie blue staining, the resulting protein profile in N-EVs indicated EVs-NMVs fusion (Fig. 2D). Additionally, WB results demonstrated that N-EVs inherited intercellular adhesion molecules (PSGL-1, CD11b) and cytokine receptors (TNFR1, IL-6R) from NMVs (Fig. 2E). Although N-EVs inherited most RNA content from EVs, the RNA concentration of N-EVs was slightly lower than that of EVs. However, the difference was not statistically significant and could be attributed to the loss of contents during extrusion. (Fig. 2F). Collectively, these findings indicated the successful fusion of EVs and NMVs via extrusion, resulting in the generation of N-EVs that inherited characteristic components from both EVs and NMVs.

2.3. Ex and in vivo targeting capabilities of N-EVs

During renal IRI, leukocytes, particularly NEs, are first recruited to the injured ECs through interactions involving adhesion molecules, such as PSGL-1, playing a critical role in the initial leukocyte capture process [14,16]. Subsequently, these leukocytes migrate to the renal parenchyma, initiating severe inflammatory responses.

Herein, we investigated the targeting capability of N-EVs toward injured HRGECs. Following H/R treatment, fluorescence microscopy images revealed elevated expression of P-selectin and E-selectin on HRGECs, both are capable of binding to PSGL-1 (Fig. 3A) [14]. After incubating DID-labeled EVs, N-EVs, and PSGL-1-blocked N-EVs with normoxia-treated or H/R-treated HRGECs for 2 h, immunofluorescence images demonstrated several key findings: (1) H/R-treated HRGECs internalized more N-EVs compared to normoxia-treated HRGECs; (2) N-EVs were internalized to a greater extent than EVs by H/R-treated HRGECs; and (3) blocking PSGL-1 on N-EVs membranes significantly reduced internalization by H/R-treated HRGECs (Fig. 3B and C). Flow cytometry and fluorescence imaging further corroborated these observations (Fig. 3D and E). These results suggested that the fused N-EVs could effectively target injured ECs through PSGL-1.

Furthermore, we evaluated the renal targeting efficacy of N-EVs in IRI rats. Fluorescence imaging of IRI kidneys revealed that the radiant efficiency was highest at 12 h post intravenous injection of N-EVs compared to other time points (6, 24, and 72 h) (Fig. S3). Consequently, all subsequent experimental measurements were conducted at 12 h post-reperfusion. As shown in Fig. 4A, P-selectin expression markedly increased in the IRI kidneys. Fluorescence imaging of isolated organs demonstrated that DID-labeled EVs and N-EVs mainly accumulated in the livers, lungs, and kidneys. Notably, renal IRI significantly increased the recruitment of N-EVs to the kidneys compared to the Sham group. In IRI kidneys, additionally, the fluorescence intensity associated with N-EVs was approximately 2.51 times higher than that observed with EVs (Fig. 4D). In the control groups solely injected with DID dye, the DID dye predominantly accumulated in the lungs and liver, with no significant accumulation observed in the kidneys. This finding suggests that the distribution pattern described in our study is specific to N-EVs and is not attributable to dye aggregation (Fig. S4). Moreover, renal fluorescence images confirmed that the blockade of PSGL-1 severely impaired the ability of N-EVs to target injured kidneys, nevertheless it remained higher than that of EVs, which might be attributed to the involvement of other adhesion molecules (Fig. 4E). Immunofluorescence images of frozen kidney sections further supported these findings and revealed the superior endothelial targeting ability of N-EVs (Fig. 4B and C). The *in vivo* tracking outcomes further confirmed the targeting efficacy of N-EVs in IRI kidneys and underscored the significance of PSGL-1 in facilitating this targeting capability.

2.4. N-EVs reversed renal microvascular dysfunction

The kidneys are among the most highly perfused organs in the body. Microvascular dysfunction contributes to impaired reparative angiogenesis and vascular rarefaction, initiating and worsening renal IRI. Therefore, repair of the injured microvascular system is essential for renal IRI.

In the H/R HRGECs model, N-EVs notably enhanced cell proliferation compared to the EVs group (Fig. 5A). Furthermore, N-EVs rescued the tube formation and migratory capacities of injured HRGECs. The total branching length significantly increased in the presence of N-EVs, while the wound area decreased significantly (Fig. 5B and C). Immunohistochemical analysis of renal paraffin sections taken 24 h after tail vein injection revealed a notable increase in MVD in the N-EVs group than the other groups (Fig. 5D and E). Concurrently, analysis of angiogenesis-related gene expression in renal tissues demonstrated that N-EVs significantly promoted angiogenesis in injured kidneys (Fig. 5F).

2.5. N-EVs reduced renal inflammation

Renal IRI causes significant damage to renal ECs and tubular epithelial cells, characterized by increased intercellular permeability and the release of various cytokines. These alterations lead to a massive infiltration of circulating leukocytes and cause an inflammatory cascade [25,26]. As illustrated in Fig. 6A, H/R-treated HK-2 cells produced a pronounced increase in secreted cytokines. Upon treatment with PBS, EVs, or N-EVs, it was observed that both EVs and N-EVs significantly attenuated the cytokine release from H/R-treated HK-2 cells, with N-EVs demonstrating a more pronounced effect (Fig. 6B).

Furthermore, TEER measurements revealed that H/R treatment significantly decreased TEER levels in HRGECs, indicating a disruption of endothelial integrity. However, the administration of PBS, EVs, or N-EVs ameliorated the TEER levels of injured HRGECs to varying extents, with N-EVs showing the most substantial improvement (Fig. 6D).

Giemsa staining of kidney sections demonstrated fewer infiltrating leukocytes in the N-EVs group compared to the EVs group (Fig. 6C, E). Additionally, we collected kidney supernatants from each group and conducted ELISA, revealing that N-EVs significantly reduced inflammatory cytokine levels in IRI kidneys (Fig. 6F). Researches have reported that EPCs-derived EVs could attenuate apoptosis of injured HK-2 cells, which might partly account for the reduction in NEs infiltration

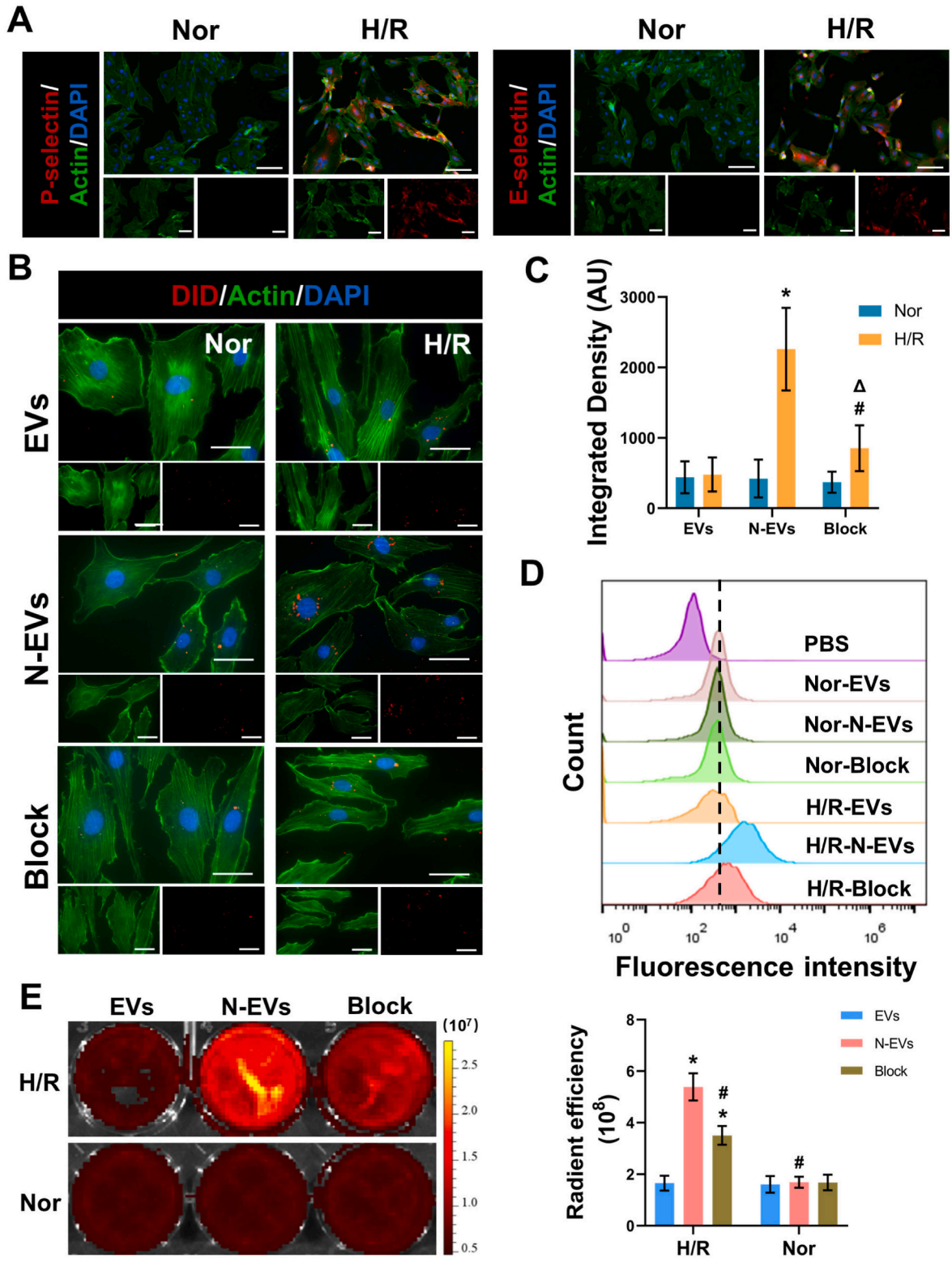

Fig. 3. Endothelial targeting ability of N-EVs *in vitro*. (A) Immunofluorescence images of P- and E-selectin expression in normoxia or H/R-treated HRGECs. Scale bar = 50 μm. (B) Representative immunofluorescence images and (C) related statistics analysis of HRGECs bound with DID-labeled EVs, N-EVs, or anti-PSGL-1 antibody-blocked N-EVs after normoxia or H/R treatment. Scale bar = 20 μm $^{*}P < 0.05$ vs. Nor N-EVs; $\#P < 0.05$ vs. Nor Block; $\Delta\ P < 0.05$ vs. H/R N-EVs. (D) Flow cytometry results and (E) Fluorescence imaging analysis of HRGECs bound with DID-labeled EVs, N-EVs, or anti-PSGL-1 antibody-blocked N-EVs after normoxia or H/R treatment. $^{*}P < 0.05$ vs. H/R EVs; $\#P < 0.05$ vs. H/R N-EVs.

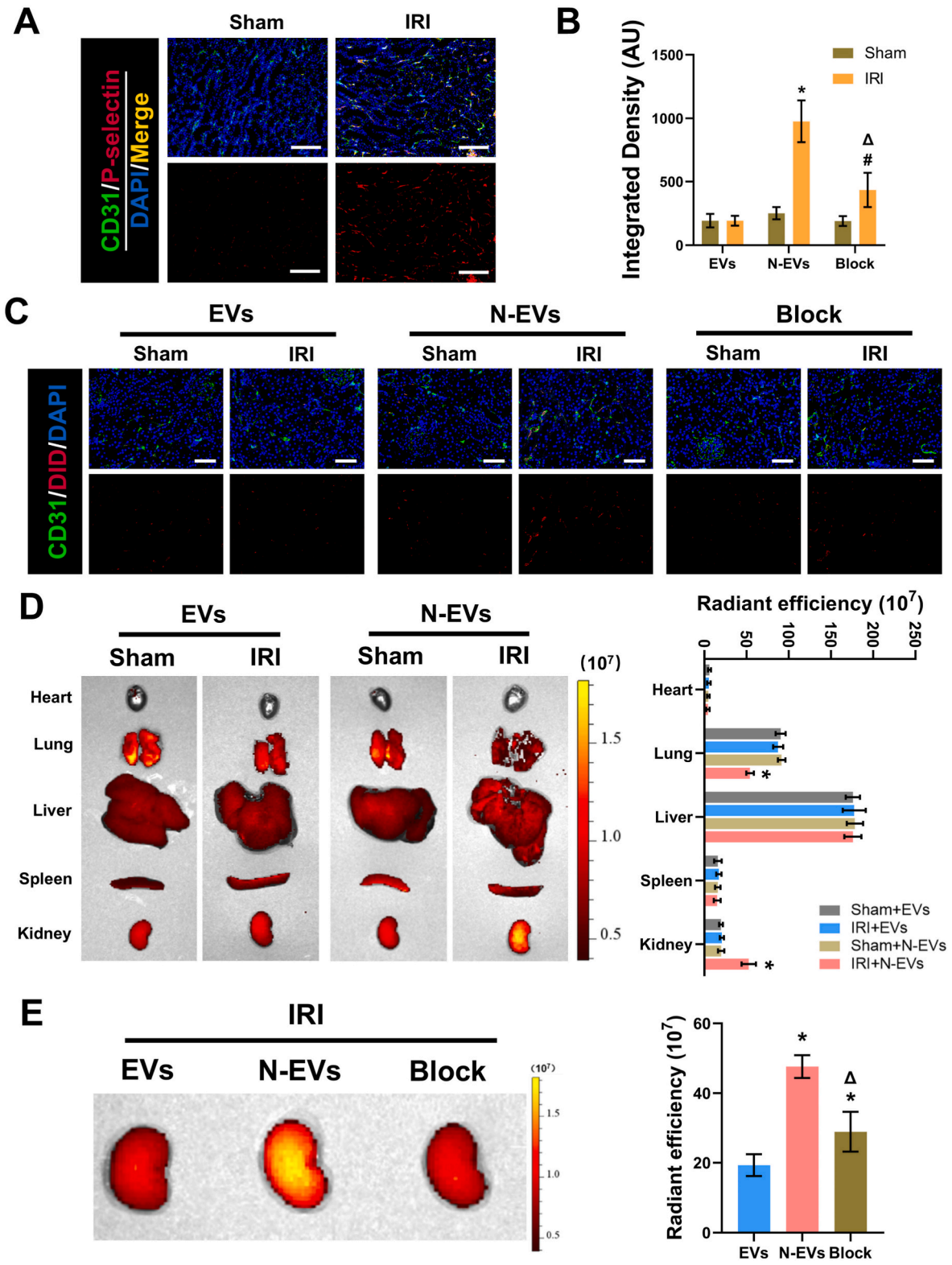

Fig. 4. Renal targeting ability of N-EVs *in vivo*. (A) Representative immunofluorescence images of P-selectin expression in Sham or IRI kidneys. Scale bar = 200 μm. (C) Fluorescence microscopy and (B) related statistics analysis of DID-labeled EVs, N-EVs, or anti-PSGL-1 antibody-blocked N-EVs in Sham or IRI kidneys. Scale bar = 100 μm *P < 0.05 vs. Sham + EVs; #P < 0.05 vs. Sham + Block; Δ P < 0.05 vs. IRI + N-EVs. (D) Fluorescence imaging and quantification analysis of DID-labeled EVs or N-EVs in the major organs of Sham or IRI group. *$P < 0.05$ vs. IRI + EVs. (E) Fluorescence imaging and quantification analysis of DID-labeled EVs, N-EVs, or anti-PSGL-1 antibody-blocked N-EVs in IRI kidneys. *$P < 0.05$ vs. EVs; Δ $P < 0.05$ vs. N-EVs.

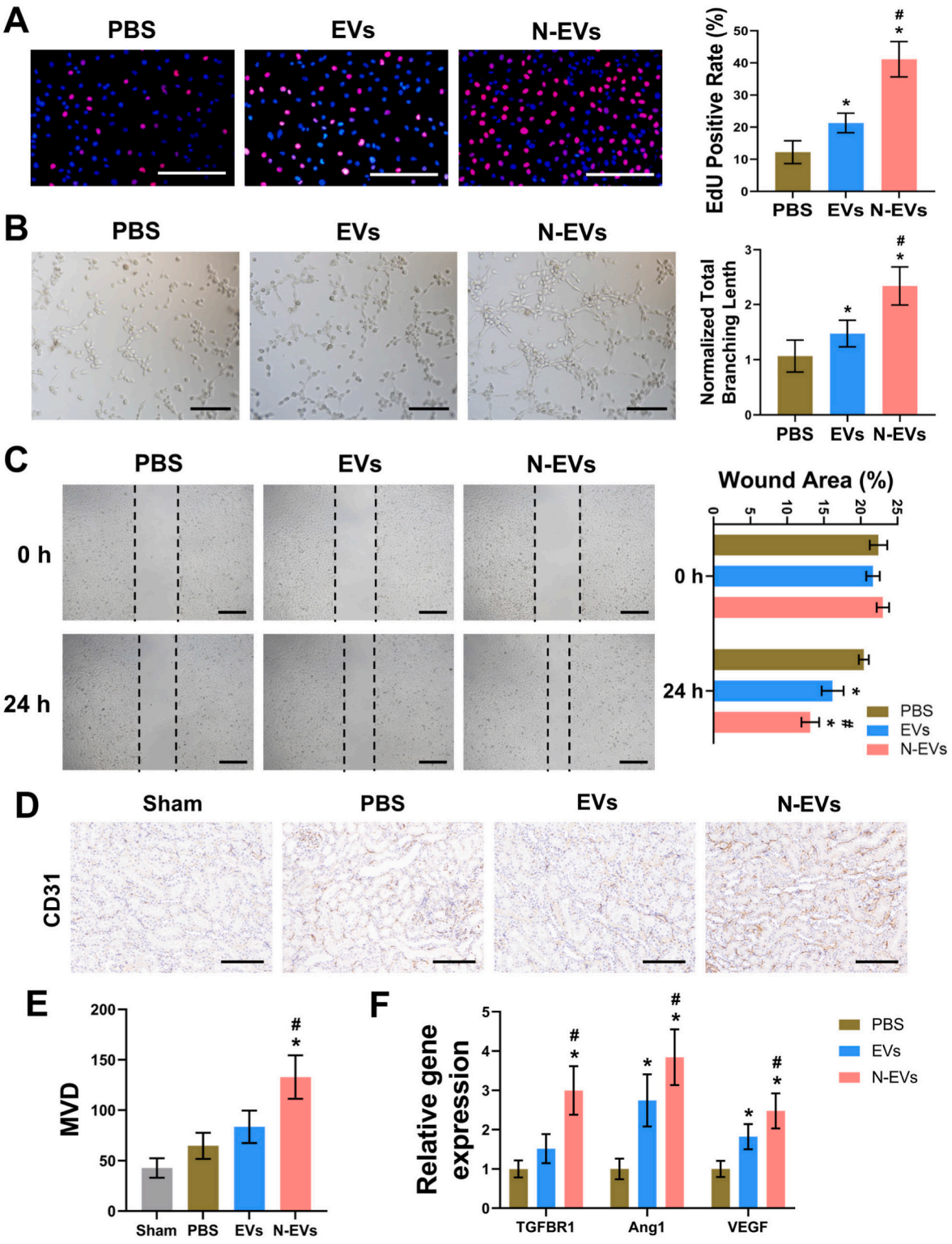

Fig. 5. N-EVs reverse endothelial damage repair and promote renal angiogenesis. Representative images and statistics analysis of (A) EdU method, (B) tube-formation assay, (C) and scratching assay for evaluating the proliferation, angiogenesis, and migration capability of H/R HRGECs treated with PBS, EVs, and N-EVs. (D) Representative CD31 immunohistochemical staining images and (E) MVD analysis in the sham, PBS, EVs, N-EVs group. (F) Quantification of angiogenesis-related genes in H/R-treated HRGECs of each group by qRT-PCR. Scale bar = 200 μm *$P < 0.05$ vs. PBS; #$P < 0.05$ vs. EVs.

within the EVs group [11]. Furthermore, chemokine receptors (e.g. TNFR1, IL-6R) were confirmed to express on N-EVs, which could counteract chemokines produced by injured HK-2 cells, further diminishing NEs migration [27]. These findings suggest that N-EVs may play a vital role in inhibiting leukocyte infiltration and reducing inflammatory cytokine levels in the IRI kidneys.

2.6. N-EVs improved renal function and parenchymal repair

BUN and Scr are vital serum markers for assessing renal function [3].

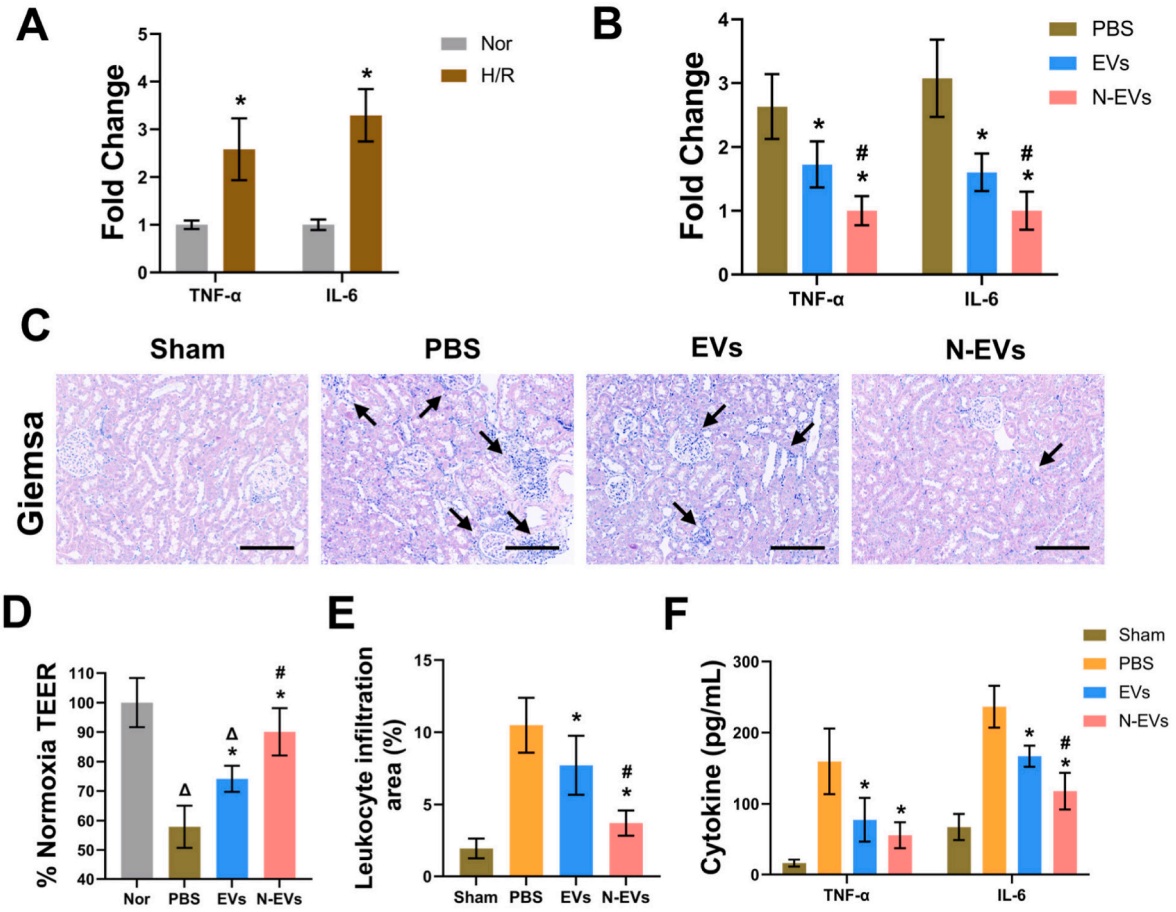

Fig. 6. Anti-inflammatory effects of N-EVs. (A) Inflammatory cytokine levels of normoxia or H/R treated HK-2 cells and (B) PBS, EVs, or N-EVs treated H/R HK-2 cells by ELISA. (C) Representative Giemsa staining images and (E) statistics analysis in each group to evaluate leukocyte infiltration (black arrows, leukocytes). (D) Statistical analysis of TEER in each group (percentage of normoxia-treated HRGECs) to assess the integrity of HRGECs. (F) Inflammatory cytokine levels of renal tissues in each group by ELISA. Scale bar = 200 μm *$P < 0.05$ vs. PBS; #$P < 0.05$ vs. EVs; Δ $P < 0.05$ vs. Nor.

As depicted in Fig. 7A, intravenous administration of EVs markedly reduced renal BUN and Scr levels at 1 day and 7 days after reperfusion, while N-EVs demonstrated a stronger renoprotection. Subsequently, we conducted HE staining of renal sections from each group to evaluate renal histopathology at 1 day and 7 days post intravenous injection of EVs or N-EVs. The findings revealed renal injury characterized by dilatation of renal tubules and Bowman's capsule, tubular necrosis, loss of brush border, and protein tubular formation following the IRI procedure. Notably, compared to EVs, N-EVs significantly mitigated renal injury at both 1 day and 7 days after IRI (Fig. 7B, E). PCNA immunohistochemistry demonstrated an increase in the proportion of PCNA-positive cells at 1-day post-IRI in the EVs group compared to the PBS group, with the highest proportion observed in the N-EVs group (Fig. 7C, F). TUNEL staining revealed increased apoptosis in kidney cells following IRI; however, N-EVs significantly attenuated the proportion of apoptotic cells in the kidney to a greater extent than EVs (Fig. 7D, G). These results indicated that N-EVs significantly enhanced renal function, mitigated renal injury, and promoted renal parenchymal repair after IRI.

2.7. MiRNA expression and cargo delivery in N-EVs

Research indicated that EPCs-derived EVs exert their functions by delivering various biologically active components, particularly miRNAs [9]. To investigate the potential mechanisms underlying the beneficial effects of N-EVs on renal IRI, we conducted miRNA sequencing of both EVs and N-EVs. The results revealed a similar miRNA expression profile between EVs and N-EVs, with miR-21-5p being the most abundantly expressed miRNA in both two types (Fig. 8A). Notably, miR-21-5p accounted for 29 % of the total miRNA expression in N-EVs (Fig. 8C). Subsequently, we validated the expression of the top three miRNAs in EVs and N-EVs using qPCR. Consistently, miR-21-5p exhibited significantly higher expression levels in both EVs and N-EVs compared to other miRNAs (Fig. 8D). Interestingly, although there was a trend of lower miRNA expression in N-EVs compared to corresponding EVs, which might be attributed to cargo loss during membrane fusion extrusion, this difference was not statistically significant. However, the modified NMVs enhanced the targeting capability of N-EVs, compensating for this potential limitation. Importantly, compared to EVs, N-EVs demonstrated enhanced delivery of miR-21-5p to H/R treated HRGECs and IRI kidneys (Fig. 8E).

Following these findings, we directed our subsequent investigations toward miR-21-5p. Gene Ontology (GO) analysis revealed the broad involvement of miR-21-5p in regulating biological processes such as cell proliferation, apoptosis, and angiogenesis. Kyoto Encyclopedia of Genes and Genomes (KEGG) analysis identified highly enriched pathways associated with miR-21-5p (Fig. 8B). Previous studies have highlighted that EPC-derived EVs can enhance vascular repair and decrease cell apoptosis by delivering miR-21-5p [10,28]. To explore the specific role of miR-21-5p, we prepared EPCs-derived $EVs^{Anta\text{-}miR-21-5p}$ and $N\text{-}EVs^{Anta\text{-}miR-21-5p}$ by transfecting Anta-miR-21-5p into EPCs (Fig. 8F and G). Our results demonstrated a significant reduction in miR-21-5p delivery to H/R-treated HRGECs and IRI kidneys (Fig. 8H).

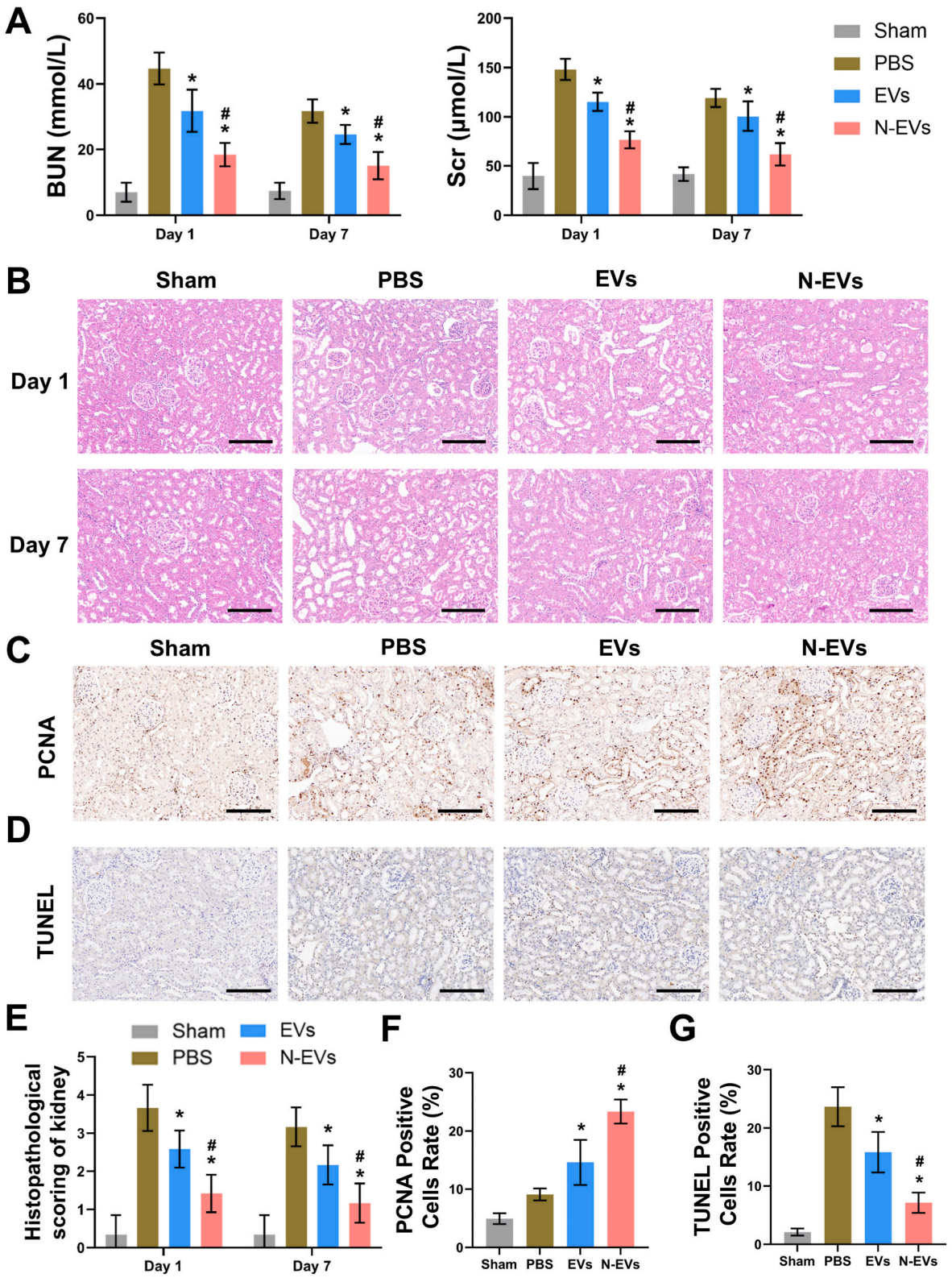

Fig. 7. Effects of N-EVs on renal function and parenchymal repair. (A) BUN and Scr at 1 day and 7 days after renal IRI. (B) Representative HE-stained images and (E) histopathological scoring of the kidneys at 1 day and 7 days after IRI. (C) Representative PCNA-stained images and (F) statistics analysis of kidneys 1 day after IRI. (D) Representative TUNEL-stained images and (G) statistics analysis of kidneys at 1 day after IRI. Scale bar = 200 μm *$P < 0.05$ vs. PBS; #$P < 0.05$ vs. EVs.

2.8. *N-EVs exert renoprotective effects by delivering miR-21-5p*

In vitro experiments revealed that N-EVs$^{\text{Anta-miR}-21-5p}$ exhibited diminished capacity compared to N-EVs$^{\text{Anta-NC}}$ in promoting cell proliferation and migration, and tube formation (Fig. 9A and B; S5A). Matrigel plug assays also showed that antagomiR-21-5p attenuated the ability of N-EVs to promote angiogenesis (Fig. 9E, F, G). Moreover, MVD was notably reduced in IRI kidneys treated with N-EVs$^{\text{Anta-miR}-21-5p}$

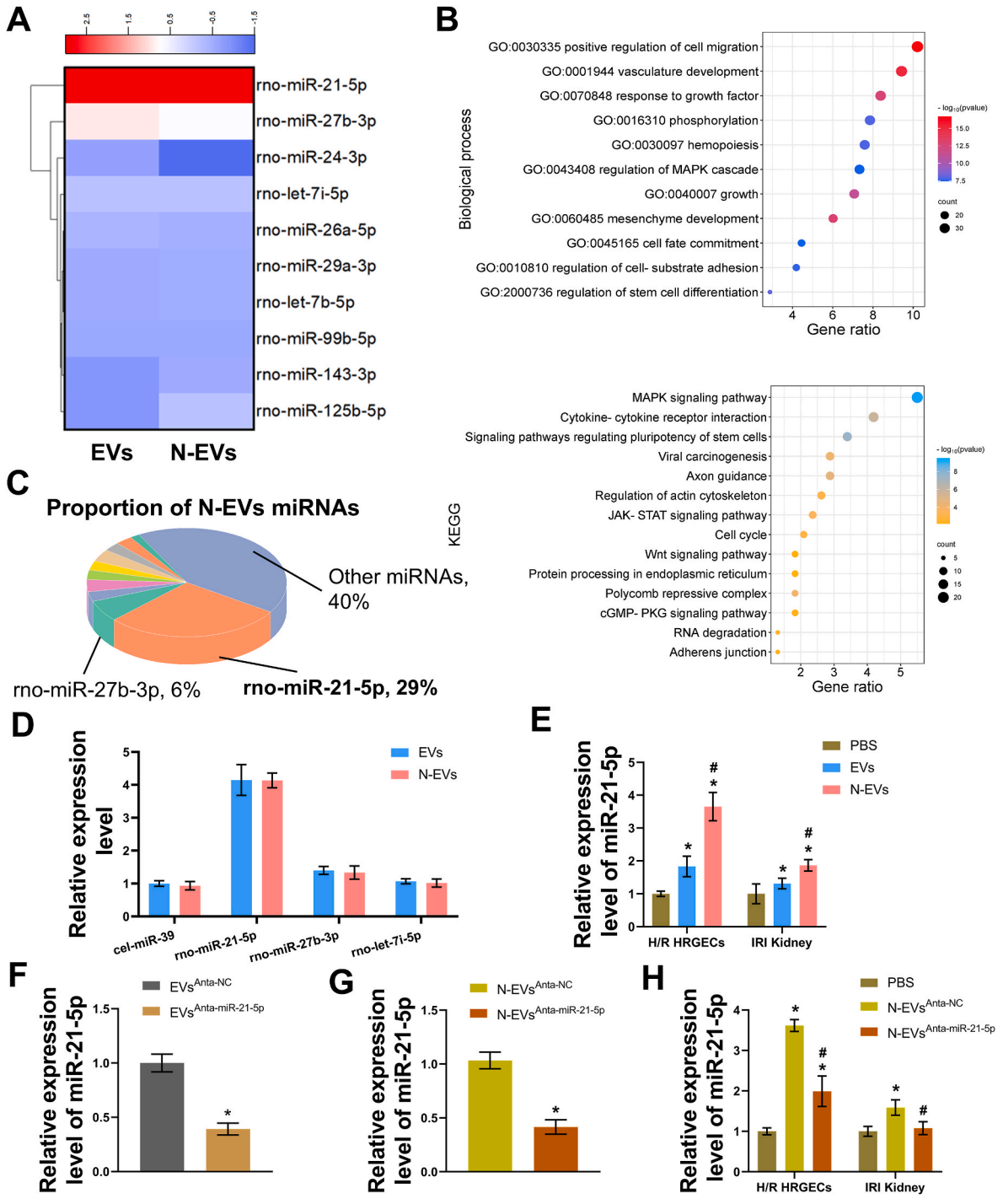

Fig. 8. The miRNA analysis of N-EVs. (A) Heatmap of top 10 miRNAs in EVs and N-EVs group (red represented high expression). (B) Gene ontology functional clustering of miR-21-5p predicted target genes involved in biological processes (Above). KEGG pathway enrichment analysis indicated the highly enriched pathways for miR-21-5p predicted target genes (Below). (C) Proportional distribution of N-EVs miRNAs. (D) Top 3 miRNA expression quantification in EVs or N-EVs group by qRT-PCR (cel-miR-39 served as the external control). *P < 0.05 vs. PBS; #P < 0.05 vs. EVs. Quantification analysis of miR-21-5p expression in (E) H/R HRGECs and IRI kidneys treated with PBS, EVs, or N-EVs; (F) EVs and (G) N-EVs after miR-21-5p knockdown; and (H) in H/R HRGECs and IRI kidneys treated with PBS, N-EVs$^{Anta\text{-}NC}$, or N-EVs$^{Anta\text{-}miR-21-5p}$ by qRT-PCR. *P < 0.05 vs. PBS; #P < 0.05 vs. N-EVs$^{Anta\text{-}NC}$.

(Fig. 9C). Further analysis of kidney sections showed increased renal injury pathology score, reduced percentage of PCNA-positive cells, and increased percentage of TUNEL-positive cells in the N-EVs$^{Anta\text{-}miR-21-5p}$ group compared to N-EVs$^{Anta\text{-}NC}$ (Fig. 9D; S5B, C). These findings suggested that the reduced delivery of miR-21-5p by N-EVs attenuated their protective effects on injured kidneys.

2.9. *In vivo* safety analysis of N-EVs

To evaluate the clinical translational safety of N-EVs, we conducted an *in vivo* safety analysis. Rats were administered intravenous EVs or N-EVs once a week, and their blood and major organs were collected after 4 weeks for analysis. Our findings revealed that neither EVs nor N-EVs induced histopathological changes to the major organs (heart, lung,

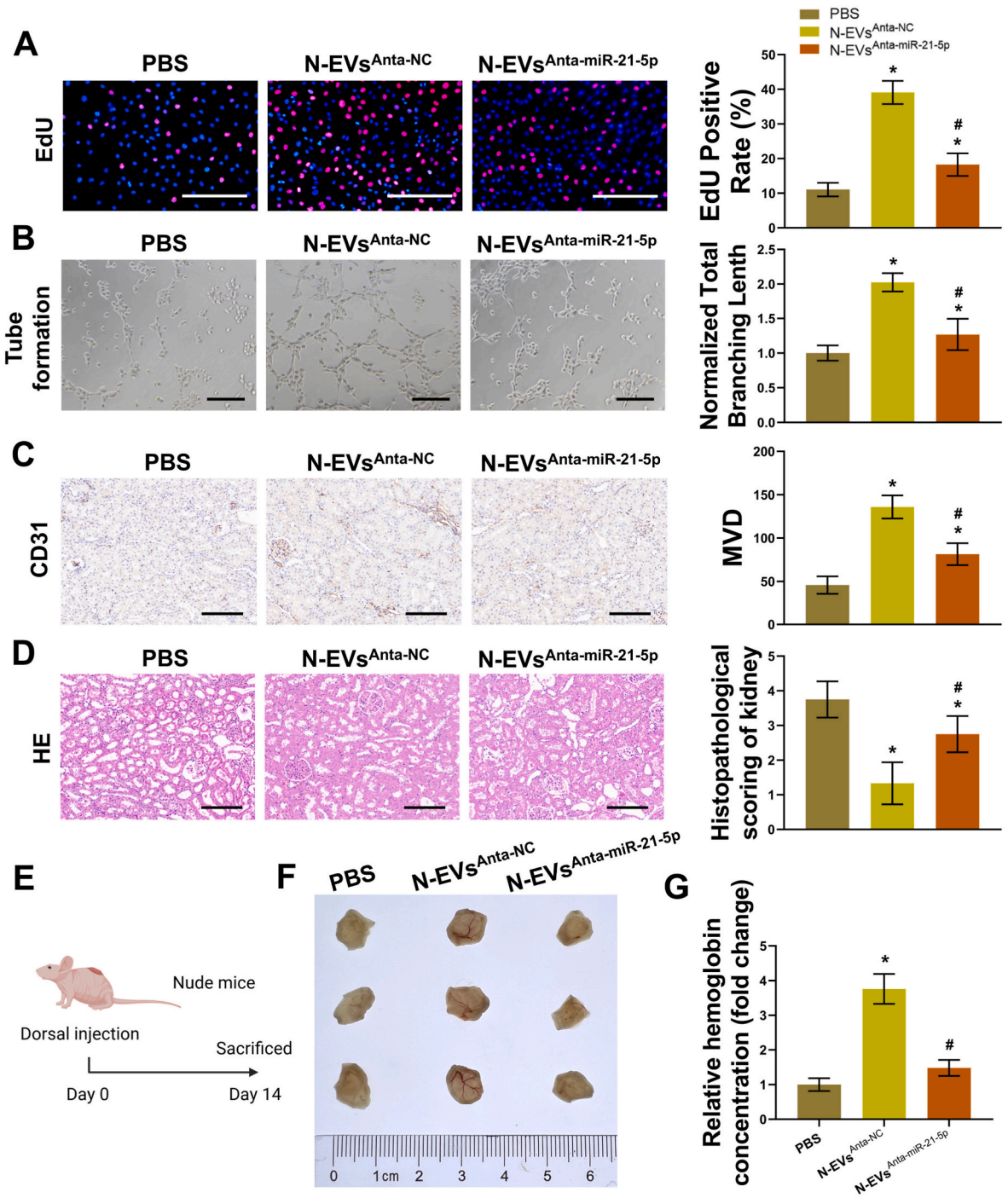

Fig. 9. Effects of miR-21-5p in N-EVs on H/R HRGECs and IRI kidneys. (A) Representative images and statistics analysis of (A) EdU and (B) tube-formation assay in H/R HRGECs. Representative (C) CD31-stained and (D) HE-stained images of kidneys at 1 day after IRI. (E) Schematic diagram of the process of subcutaneous Matrigel plug model *in vivo*. (F) Gross observation of the Matrigel plugs. Scale bar = 200 μm. (G) Relative hemoglobin concentration in three groups of Matrigel plugs. $^{*}P < 0.05$ vs. PBS; $^{\#}P < 0.05$ vs. N-EVs$^{\text{Anta-NC}}$.

liver, spleen, kidney) of rats (Fig. S6A). Furthermore, N-EVs did not impair the cardiac, hepatic, as well as renal function of rats (Fig. S6B). Importantly, there was no significant elevation of serum cytokines in rats injected with N-EVs, suggesting that they did not elicit acute inflammatory responses in rats (Fig. S6C). Considering the potential risk of thrombosis associated with the *in vivo* use of nanomaterials, coagulation tests demonstrated that N-EVs did not affect the coagulation function of rats (Fig. S6D). These results collectively underscore the safety profile of N-EVs and support their promising clinical application.

3. Discussion

EPCs are mainly sourced from bone marrow, peripheral blood, and adipose tissues. So far, EPCs have been demonstrated to promote injury repair, especially addressing vascular dysfunction, under both physiologic and pathological conditions [23]. Despite their therapeutic potential, the clinical application of EPCs is hindered by cellular immune rejection, infusion toxicity, and potential tumorigenicity [29]. In recent years, there has been growing interest in the beneficial effects of EVs derived from EPCs across various diseases, including AKI, acute lung

injury, stroke, and myocardial infarction [9]. However, before these EVs-based therapies can be translated into clinical practice, it is imperative to maximize their therapeutic efficacy. One key challenge facing stem cell-derived EVs that needs to be urgently addressed is their low homing efficiency.

The kidney, characterized by a complex and extensive vascular network, is one of the most highly perfused organs. During renal IRI, inflamed ECs and tubular epithelial cells release various cytokines into circulation, activating circulating leukocytes [5]. Concurrently, the expression of adhesion molecules on the ECs surface is markedly elevated [30,31]. NEs, as the most abundant and rapidly responsive leukocytes during inflammation, play a pivotal role in renal IRI. Heightened expression of adhesion molecule ligands and chemokine receptors on the surface of NEs facilitates a chain of inflammatory responses including tethering, rolling, adhesion, and transmigration [14,32]. Specifically, NEs initially bind to P-selectin and E-selectin on injured endothelium via the high expression of PSGL-1 [16]. This binding prompts a transition from a laminar state to adherence to the endothelium and represents a critical step in leukocyte adhesion during inflammation. Thus, the NEs-derived membrane could be an effective 'ornament' to enhance the endothelium targeting of EVs.

In this study, we developed a novel engineered nanovesicle termed N-EVs by fusing NMVs with EPCs-derived EVs using a straightforward physical method involving ultrasonication and extrusion. Notably, NEs and EPCs were both extracted from rat peripheral blood, which represents an easily accessible source for future clinical applications. The prepared NMVs from NEs displayed high levels of adhesion molecules including PSGL-1 and CD11b, which was consistent with findings reported by Han et al. [33] Following the fusion of NEs-derived NMVs with EPCs-derived EVs, the resulting N-EVs exhibited a shape similar to that of EVs and displayed a more uniform diameter distribution. Furthermore, N-EVs possessed good suspension stability in various solvents, including 10 % human plasma and PBS, indicating favorable prospects for *in vivo* applications. To confirm the successful fusion, we employed multiple analytical techniques including immunofluorescence, ELISA, SDS gel, and Western blotting. These results verified that N-EVs retained the promising therapeutic effects of EVs along with the active membrane proteins from NEs.

Both *in vivo* and *in vitro* experiments demonstrated the enhanced targeting efficacy of N-EVs compared to EVs towards H/R HRGECs or IRI kidneys. Notably, blocking PSGL-1 expression on the surface of N-EVs using an anti-PSGL-1 antibody significantly reduced their targeting capability. This underscored the superior targeting capacity of N-EVs towards injured endothelium and kidneys and emphasized the pivotal role of PSGL-1 in this chemotactic effect. Interestingly, even after blocking PSGL-1 expression, the targeting ability of N-EVs remained stronger than that of EVs, possibly due to the presence of other adhesion molecule receptors inherited from NEs on N-EVs.

Furthermore, N-EVs markedly enhanced the proliferation, migration, and tube-forming capability of H/R-treated HRGECs and promoted angiogenesis in IRI kidneys. Chen et al. highlighted the potential of neutrophil membrane-modified nanoparticles to ameliorate the inflammatory microenvironment in myocardial infarction and emphasized the anti-inflammatory role of chemokine receptors [32]. Similarly, our engineered N-EVs expressed typical chemokine receptors TNFR1 and IL6R. In the *in vitro* Transwell model, N-EVs markedly restored the endothelial integrity of damaged HRGECs. Additionally, N-EVs significantly suppressed cytokine release from injured HK-2 cells, potentially due to the neutralization of cytokines by surface chemokine receptors on the N-EVs. The binding of N-EVs to damaged endothelium may block the adhesion molecule binding sites on ECs, thereby inhibiting the adhesion of circulating leukocytes. These findings suggest that N-EVs possess a robust capability to inhibit leukocyte infiltration and mitigate local inflammatory responses. Additionally, treatment with N-EVs led to a significant decrease in leukocyte infiltration and cytokine levels in the IRI kidneys. Subsequent comprehensive assessments of renal function and parenchymal injury demonstrated that N-EVs exhibited a significantly stronger capacity for injury repair compared to EVs.

MiRNAs are prominent components of EVs and serve as a crucial mechanism underlying their biological effects [34]. Analysis through miRNA sequencing and qPCR revealed highly similar miRNA expression profiles between EVs and N-EVs, both containing substantial levels of miR-21-5p. MiR-21-5p has been extensively studied in various disease models and demonstrated to promote vascular and renal repair, particularly in AKI [10,28,35]. Therefore, our subsequent studies were focused on miR-21-5p. We found that compared with EVs, the total RNA and miR-21-5p content of N-EVs tended to decrease, but not yet statistically significant. This might be due to the rupture of EVs during sonication and subsequent extrusion, resulting in the loss of relevant contents. Nevertheless, our results further revealed that N-EVs could deliver more miR-21-5p than EVs to the injured HRGECs and kidneys, which might be attributed to the markedly elevated targeting ability. To further explore the role of miR-21-5p delivered by N-EVs, we prepared N-EVs$^{\text{anta-miR}-21-5p}$. As expected, the delivery of miR-21-5p by N-EVs to the ECs and kidneys was significantly reduced after being treated with anta-miR-21-5p. Furthermore, the capacity of N-EVs$^{\text{anta-miR}-21-5p}$ to repair injured ECs and kidneys was notably diminished compared to N-EVs$^{\text{anta-NC}}$. These findings underscored the critical role of N-EVs in promoting angiogenesis and repairing renal IRI primarily through delivery of miR-21-5p. Additionally, following sustained high-dose administration in rats, N-EVs were demonstrated to be absent of toxic side effects on major organs and their functions, thereby confirming their safety and biocompatibility for potential therapeutic applications.

However, this study has certain limitations. Specifically, we have not yet examined the long-term outcomes of N-EVs *in vivo*. Furthermore, leukocyte adhesion is a complex biological process and the roles of other adhesion molecules of N-EVs on endothelium targeting have not been fully explored.

4. Conclusion

In summary, our study presented an innovative EVs engineering approach that combined the innate targeting capabilities of NEs with the biological functions of EVs. The resulting N-EVs inherited the tropism of NEs to the injured endothelium of IRI kidneys and could provide effective nephroprotection by delivering miR-21-5p sourced from EVs. Moreover, N-EVs exhibited notable anti-inflammatory properties. This engineered membrane fusion strategy held promise for leveraging various sources of EVs and cell membranes to develop nanomedicines tailored for diverse diseases.

5. Experimental section

5.1. Isolation and characterization of NEs and EPCs

Rat peripheral blood NEs were isolated following the manufacturer's protocol (LZS1091, tbdscience, China). Briefly, the collected rat peripheral blood samples were proportionally mixed with erythrocyte sediment and carefully layered onto the gradient interface in a 15 mL centrifuge tube. The mixture was centrifuged at 800 g for 20 min. The resulting lower creamy white cell layer was NEs. These NEs were then transferred to a new centrifuge tube and washed three times with the provided wash solution. Finally, an optimal amount of erythrocyte lysate buffer was introduced to further purify NEs. The NEs were stored at −80 °C in a serum-free cell freezing medium (C40100, NCM Biotech, China). NEs were characterized by flow cytometry using two antibodies, anti-CD11b-FITC (561684, BD Bioscience, USA) and anti-RP-1-PE (550002, BD Bioscience, USA). A FITC-labeled Mouse IgA (553478, BD Bioscience, USA) and a PE-labeled Mouse IgG2α (349053, BD Bioscience, USA) were served as the isotype control.

EPCs were also extracted from rat peripheral blood using density centrifugation, as described in previous studies [36]. Blood samples

were initially mixed with phosphate-buffered saline (PBS; 10010023, Gibco, USA) in equal proportions and then carefully layered onto an equal volume of Ficoll-Paque (1.084 g/mL; GE Healthcare, USA). The mixture was centrifuged at 1100g for 30 min at room temperature. The mononuclear cells from the middle layer were collected, resuspended in Complete Endothelial Cell Growth Medium (EGM-2, Lonza, Switzerland), and seeded into 6-well plates pre-coated with type I rat tail collagen (Corning, USA) at a density of 1×10^6 cells/mL. After 5–7 days of incubation, non-adherent cells were washed away, and a fresh EGM-2 medium was added. The medium was subsequently changed every 3–4 days until cell colonies appeared. EPCs from passages 3 to 5 were selected for further experiments. A set of flow cytometry antibodies—anti-CD34-PE (bs-0646R-PE, Bioss, China), anti-CD133-FITC (orb15325, Biorbyt, UK), anti-VEGFR2-FITC (bs-10412R-FITC, Bioss, China), anti-CD31-APC (bs-0195R-APC, Bioss, China), anti-CD14-FITC (bs-1192R-FITC, Bioss, China), and anti-CD45-PE (bs-0522R- PE, Bioss, China)—were used for the characterization of EPCs hallmarks. Additionally, Dil-Ac-LDL (MP6013, Maokang Biotechnology, China) uptake and FITC-UEA-1 (MP6308, Maokang Biotechnology, China) binding assays were used for further confirmation of EPCs by immunofluorescence microscopy.

5.2. Isolation of EPCs-derived EVs and NEs membrane

After reaching 80 % confluency, EPCs were re-cultured in serum-free EGM-2 media for 24 h. Then the conditioned media were collected and sequentially centrifuged at 300 g, 2000 g, and 10,000 g for 10 min at 4 °C to remove cells, cell debris, and apoptotic vesicles. Subsequently, the supernatant was subjected to ultracentrifugation at 100,000 g for 70 min at 4 °C using an Optima XPN-ultracentrifuge (Beckman Coulter, USA), yielding the EVs pellet. The EVs were then washed once with PBS, ultracentrifuged again, resuspended in PBS, and stored at −80 °C. Quantification of EVs was performed using a BCA Protein Assay Kit (WB6501, NCM Biotech, China).

NEs membranes were extracted following a modified version of previously established protocols [37]. NEs were homogeneously suspended in a lysis buffer composed of 225 mM D-mannitol, 75 mM sucrose, 30 mM Tris-HCl (pH = 7.5), 0.2 mM EGTA, and a protease-phosphatase inhibitor mixture. The cells were then disrupted by repeated grinding (at least 20 passes) using a Dounce homogenizer with a tight-fitting pestle. The homogenized solution was initially centrifuged at 800 g for 10 min at 4 °C. The supernatant was collected and centrifuged again at 10,000 g for 20 min at 4 °C, and the resulting pellet was discarded. The supernatant was then subjected to further centrifugation at 100,000 g for 40 min at 4 °C. The obtained membrane pellet was washed twice with 0.2 mM EDTA solution. The extracted membrane was quantified using a BCA Protein Assay Kit (WB6501, NCM Biotech, China). The membrane was suspended in a 0.2 mM EDTA solution and stored at −80 °C.

5.3. Preparation of $EPCs^{Anta-NC}$, $EPCs^{Anta\text{-}miR-21-5p}$, $EVs^{Anta-NC}$, and $EVs^{Anta\text{-}miR-21-5p}$

MiRNA antagomir is a miRNA inhibitor with specific chemical modifications. According to the manufacturer's instructions, miRNA antagomir negative control (NC) and miRNA-21-5p (miR-21-5p) antagomir were transfected into well-maintained EPCs of passages 3 to 5 using Lipofectamine™ 3000 (L3000150, Invitrogen, USA) and were designated as $EPCs^{Anta-NC}$ or $EPCs^{Anta\text{-}miR-21-5p}$, respectively. Correspondingly, EVs originating from $EPCs^{Anta-NC}$ or $EPCs^{Anta\text{-}miR-21-5p}$ were labeled as $EVs^{Anta-NC}$ or $EVs^{Anta\text{-}miR-21-5p}$, respectively. The sequence of miRNA antagomir NC was: 5′-CAGUACUUUUGUGUAGUACAA-3′; miR-21-5p antagomir was: 5′-UCAACAUCAGUCUGAUAAGCUA-3′.

5.4. Preparation and identification of N-EVs

For the fabrication of NMVs, NEs membranes were serially extruded through 400, 200, and 100 nm polycarbonate porous membranes 11 times using a mini extruder (Avanti Polar Lipids, USA). NMVs were then mixed with EVs at a ratio of 1:1 and sonicated for 2 min in an ice bath. The mixture was subsequently extruded through 400, 200, and 100 nm polycarbonate membranes 11 times again using the mini extruder to prepare fused N-EVs.

The morphological images of EVs, NMVs, and N-EVs were obtained using a Hitachi HT7800 transmission electron microscope (TEM) operating at 100 kV. The particle size distribution of EVs and N-EVs at days 0, 1, 3, 7, and 14 were determined using nanoparticle tracking analysis (NTA; n = 3; NanoSight, Malvern, UK). Western blotting (WB) assays were performed to detect the exosome-related hallmarks, CD9, Alix, and TSG101 of NMVs, EVs, and N-EVs. Primary antibodies used included: CD9 (20597-1-AP, Proteintech, China), Alix (12422-1-AP, Proteintech, China), and TSG101 (28283-1-AP, Proteintech, China) The colloid stability of NMVs, EVs, and N-EVs was determined by zeta potential measurements (n = 3; Zetasizer, Malvern, UK). Additionally, to assess the serum stability of nanoparticles, EVs, and N-EVs were suspended in 10 % human serum and their absorbance was measured at 590 nm within 4 h using a microplate reader (Infinite F500, Tecan, Switzerland).

5.5. Membrane fusion assessment

The membrane colocalization assay was conducted as previously described with minor modifications [38]. NMVs were labeled using DIO (2 μg/mL; excitation/emission = 484/501 nm; Biotium, USA), while EVs were labeled using DID (2 μg/mL; excitation/emission = 644/663 nm; Biotium, USA). Excess dyes were removed by centrifugation at 100,000 g for 70 min. The physical mixed or fused NMVs and EVs were observed under a fluorescence microscope (Axio Imager 2, Zeiss, Germany). Immunogold-stained transmission electron microscopy (IEM) was employed to assess PSGL-1 expression on N-EVs and the methodology was mainly based on the previous study [39,40]. EVs and N-EVs fixed with 4 % paraformaldehyde (PFA) were deposited on formvar-carbon mesh (TEM-FCF300CUUA, Merck) and washed thrice with PBS. After blocking with 5 % bovine serum albumin (BSA) for 10 min, the carbon mesh was then incubated with the anti-PSGL-1 primary antibody (ab316113, Abcam, UK) for 30 min. Following this, the carbon mesh was washed thrice with 1 % BSA and incubated with a colloidal gold-conjugated secondary antibody (G7402, Merck, USA) for 30 min. After rewashing with 1 % BSA and PBS three times, the carbon mesh was fixed and negatively stained using a 1 % glutaraldehyde solution and 4 % uranyl acetate. Finally, the carbon mesh was dried and observed under TEM.

A modified ELISA method was used to determine the presence of both PSGL-1 and CD63 on N-EVs. Firstly, PSGL-1 blocked N-EVs were prepared by incubating N-EVs with an anti-PSGL-1 antibody (A23373, ABclonal, China), and Rabbit Control IgG (AC005, ABclonal, China) was served as an isotype control. The specific experimental steps of the ELISA were referred to the manufacturer's instructions (SEA985Ra, Cloud-Clone Corp., China) with some modifications. Specifically, the biotin-conjugated anti-CD63 antibody was prepared ((ab281540 and ab210849 were conjugated to biotin using Biotin Conjugation Kit (ab201795) to produce Conjugate CD63 and Isotype Control respectively; Abcam, UK)) and chosen as the detection antibody. Finally, the optical density (OD) values of each group were detected at 450 nm using a microplate reader (Infinite F500, Tecan, Switzerland).

Total proteins from NMVs, EVs, and N-EVs were extracted using RIPA lysis buffer (P0013C, Beyotime, China) containing protease and phosphatase inhibitors. Protein concentration was determined using a BCA protein assay kit (WB6501, NCM Biotech, China). The protein components in each sample were separated by SDS-PAGE gel electrophoresis and subsequently transferred to a PVDF membrane

(03010040001, Merck, USA). After blocking for 1 h with 5 % BSA, the membranes were incubated with primary antibodies overnight at 4 °C. Primary antibodies used included: PSGL-1 (A23373, ABclonal, China), CD11b (A1581, ABclonal, China), TNFR1 (21574-1-AP, Proteintech, China), and IL-6R (23457-1-AP, Proteintech, China). The following day, the membranes were washed three times with TBST and incubated with the appropriate secondary antibodies for 1 h at room temperature. Followed by three washes with TBST, the membranes were treated with enhanced chemiluminescent (ECL) chemiluminescent reagent (P10300, NCM Biotech, China) and visualized using a luminescence image analysis system (5200, Tanon Tanon).

5.6. Cellular uptake of N-EVs in vitro

Coverslips (YA0350, Solarbio, China) were placed in 24-well plates (Corning, USA) and 1×10^5 human renal glomerular endothelial cells (HRGECs; Procell, China) were seeded per well. When the cells grew to about 80 %, they were divided into two groups: normoxia treatment and hypoxic/reoxygenated (H/R) treatment. Normoxia-treated cells were cultured under standard culture conditions (5 % CO_2 and 95 % air) in a complete medium. H/R treated cells were cultured under hypoxic conditions (94 % N_2, 5 % CO_2, and 1 % O_2) at 37 °C for 18 h, followed by reoxygenation under normoxia conditions for another 6 h.

The expression of P- and E-selectin in normoxia or H/R treated HRGECs was assessed through immunofluorescence staining, utilizing a fluorescence microscope (AXIO IMAGER A2, Zeiss, Germany). Initially, the cells were fixed with 4 % PFA and blocked with 3 % BSA for 1 h at room temperature (RT). Following this, the cells were washed three times with PBS. Diluted anti-P-selectin antibody (PA5-79973, Thermo Fisher, USA) or anti-E-selectin antibody (PA5-106911, Thermo Fisher, USA) was added to each well and the cells were incubated overnight at 4 °C. The next day, after three additional washes with PBS, a diluted secondary antibody (Ex/Em: 555/565 nm; ab150078, Abcam, UK) was applied and incubated at RT for another hour. Post-incubation, the cells underwent three more PBS washes, followed by the addition of FITC-labeled Amanita phalloides (Ex/Em: 495/520 nm; P5282, Sigma-Aldrich, China) to stain cellular actin, with a 30-min incubation at RT. Finally, the cell nuclei were stained with DAPI (P0131, Beyotime, China).

To investigate the cellular uptake of EVs, N-EVs, and blocked N-EVs by HRGECs, we employed immunofluorescence staining, flow cytometry, and fluorescence imaging. Initially, EVs, N-EVs, and blocked N-EVs were labeled with 5 μM DiD (60014, Biotium, USA) through incubation at 37 °C for 30 min. Excess dye was subsequently removed by adding PBS and centrifuging at 100,000 g for 70 min at 4 °C. The resulting pellets were ultracentrifuged again and resuspended in PBS. The quantification of DiD-labeled EVs, N-EVs, and blocked N-EVs was determined using a BCA assay. Equal amounts of these labeled vesicles were added to both normoxia and H/R-treated HRGECs, followed by a 2-h incubation at 37 °C. For immunofluorescence staining, the cells were treated with FITC-labeled Amanita phalloides (Ex/Em: 495/520 nm; P5282, Sigma-Aldrich, China) to stain cellular actin, and DAPI (P0131, Beyotime, China) to stain nuclei. The images were then observed using fluorescence microscopy. For flow cytometry analysis, collected cells from each group were detected and quantified using a flow cytometer (C40323, Beckman Coulter, USA) with data analyzed via FlowJo v.10.0 software (TreeStar, CA). For fluorescence imaging, the fluorescence intensity in each well was measured using an IVIS Spectrum *in vivo* imaging system (124262, PerkinElmer, Waltham, USA) and quantified with its appendant software (Living Image 4.5, Caliper Life Sciences, USA).

5.7. Animals and renal IRI model

SD rats (6–8 weeks old) and male BALB/c nude mice (4–6 weeks old) were used in our experiments. All animal experimental procedures were authorized by the Laboratory Animal Ethics Committee of Nanjing First Hospital and performed in conformity with the Guidelines for the Care and Use of Laboratory Animals.

After being anesthetized with sodium pentobarbital (50 mg/kg, i.p.), SD rats were operated on to excise the right kidneys through a dorsal incision, and the wound was meticulously sutured. Two weeks post-nephrectomy, the rats were randomly assigned to different treatment groups. The Sham procedure involved isolating the left renal artery without clamping, while the IRI procedure entailed isolating and clamping the left renal artery with a non-invasive vascular clamp for 50 min, followed by closure of the incision after restoration of blood flow and perfusion. Each rat was intravenously injected with 200 μL of PBS, EVs, or N-EVs (EVs or N-EVs, 2 μg/μL), depending on the group setting.

To examine the expression level of P-selectin in kidneys, two groups of randomly assigned rats were subjected to either the Sham or IRI procedure. Kidneys from both groups were harvested 12 h post-reperfusion. The excised kidneys were promptly frozen in the OCT compound (Tissue-Tek, Sakura Finetek, Japan) at −80 °C and subsequently sectioned into 5-μm cryosections using a cryostat (CM1950, Leica, USA). After rewarming, fixation, and sealing, the sections were incubated with an anti-CD31 primary antibody (MA5-16951, Invitrogen, USA) and an anti-P-selectin antibody (PA5-79973, Thermo Fisher, USA) at 4 °C overnight. The following day, the primary antibody was conjugated with corresponding secondary antibodies (Ex/Em: 493/528 nm; ab97239, Abcam, UK; Ex/Em: 555/565 nm; ab150078, Abcam, UK). Cell nuclei staining was performed using DAPI (C1005, Beyotime, China), and the expression of P-selectin was observed under a fluorescence microscope (AXIO IMAGER A2, Zeiss, Germany).

5.8. In vivo distribution of N-EVs

SD rats undergoing right nephrectomy were randomized into different groups (n = 6). The distribution of DiD-labeled EVs, N-EVs, and blocked N-EVs was tracked in each group using *ex vivo* fluorescence imaging and fluorescence microscopy. Briefly, 12 h post-reperfusion, kidney tissues from each group were embedded in the OCT compound (Tissue-Tek, Sakura Finetek, Japan) to make 5-μm cryosections. After rewarming, fixation, and blocking, the sections were labeled with an anti-CD31 primary antibody (MA5-16951, Invitrogen, USA) and the corresponding secondary antibody (Ex/Em: 493/528 nm; ab97239, Abcam, UK). Finally, the cell nuclei were stained with DAPI, and the DiD-positive (red) areas were observed under a fluorescence microscope (AXIO IMAGER A2, Zeiss, Germany). The area of DiD-positive nanovesicles was quantified using ImageJ software (Rasband, W.S., ImageJ, U. S. National Institutes of Health, USA).

Additionally, major organs (heart, lung, liver, spleen, and kidney) were harvested at 12 h post-reperfusion from each group. To mitigate the risk of false positives due to dye aggregation, two separate groups of rats (Sham and IRI) were intravenously administered only DID dye without any vesicles. In the IRI rats injected with N-EVs, kidneys were collected at 6, 12, 24, and 72 h post-reperfusion. These organs were immediately examined using the IVIS Spectrum *in vivo* imaging system (124262, PerkinElmer, Waltham, USA), and quantified with the accompanying software (Living Image 4.5, Caliper Life Sciences, USA).

5.9. Pro-angiogenesis of N-EVs in vitro

HRGECs were seeded in 6-well plates. After reaching 80 % confluence, the cells were subjected to H/R treatment to induce cell injury. Following this, the cells were treated with either PBS, EVs, or N-EVs (either PBS, $EVs^{Anta-NC}$, or $EVs^{Anta\text{-}miR-21-5p}$) (50 μg/$10^6$ cells) and incubated for 24 h under standard conditions.

For the cell proliferation assay, pre-treated HRGECs were performed according to the manufacturer's protocol using an EdU assay kit (C0078, Beyotime, China), and EdU-positive cells were observed under a fluorescence microscope (AXIO IMAGER A2, Zeiss, Germany).

For the tube formation assay, μ-slide angiogenesis plates (81506, Ibidi, Germany) were pre-cooled at 4 °C overnight. Subsequently, 10 μL of Matrigel (354248, Corning, USA) was added to each well and allowed to solidify at 37 °C for 30 min. Following solidification, 50 μL of pre-treated HRGECs (10^4 cells/well) suspended in DMEM complete medium (Thermo Scientific, China) were added to each well and incubated under standard culture conditions for 4 h. Tube formation was then observed using an inverted microscope (IX51, Olympus, Tokyo, Japan).

For the migration assay, uniform scratches were created on a monolayer of pre-treated HRGECs using a 200 μL pipette tip. The cells were then incubated under standard conditions in the serum-free medium. The wound areas in each group were observed at 0 and 24 h using an inverted microscope (IX51, Olympus, Tokyo, Japan).

The resulting images from the above assays were analyzed and quantified using ImageJ software (Rasband, W.S., ImageJ, U.S. National Institutes of Health, USA).

5.10. Cytokine quantification

HK-2 cells (SNL-165, Sunncell, China) were cultured in 6-well plates with DMEM complete medium (Thermo Scientific, China). Upon reaching 80 % confluence, the cells were subjected to H/R treatment. For cell supernatant analysis, supernatants from each experimental group were collected and centrifuged at 300 rpm for 10 min. The resultant supernatants were then examined using TNF-α and IL-6 ELISA kits (GEH0004 and GEH0001, Servicebio, China) according to the manufacturer's instructions.

For rat kidney samples, small pieces of kidney tissue were placed in pre-cooled saline to prepare 10 % homogenates using an electric homogenizer. The homogenates were centrifuged at 3000 rpm for 10 min, and the supernatants were collected for subsequent assays. For rat blood samples, peripheral blood was collected and centrifuged at 1000g for 10 min at 4 °C to obtain the supernatants. Collected supernatants were performed according to the manufacturer's instructions (GER0004 and GER0001, Servicebio, China).

5.11. Measurement of transendothelial electrical resistance

HRGECs were seeded in 0.4 μm pore size transwell inserts (353180, Corning, USA), with DMEM complete medium added to both the upper and lower chambers. The cells were cultured under standard conditions until complete confluence. Endothelial cell permeability was evaluated by measuring transendothelial electrical resistance (TEER) using a resistance meter (EVOM, WPI, USA) according to the manufacturer's instructions. Once endothelial cell monolayers were formed (TEER $>25\ \Omega \times cm^2$), the cells were subjected to a H/R procedure. Subsequently, PBS, EVs, or N-EVs (50 μg/10^6 cells) were added to the upper chamber. After 24 h of co-culturing, TEER values were measured again. The results are reported as a percentage of the TEER values relative to the normoxia conditions.

5.12. Histological and immunohistochemical examination

Paraffin sections (5 μm) were meticulously prepared from the kidneys of each experimental group, following previously reported protocols [41]. Renal histopathology was assessed through hematoxylin and eosin (HE) staining at 1 day and 7 days post-reperfusion. The extent of tubular damage was evaluated in a blinded manner by two experienced pathologists, who assigned histological scores based on the damage severity (0: 0 %; 1: <10 %; 2: 10–25 %; 3: 26–45 %; 4: 46–75 %; 5: >75 %).

To determine leukocyte infiltration in kidney tissue, paraffin sections were stained using a modified Giemsa staining kit (G1079, Servicebio, China), adhering to the manufacturer's instructions. Additionally, cell proliferation and angiogenesis in renal tissues were assessed 1 day after reperfusion using proliferating cell nuclear antigen (PCNA) and CD31 staining, respectively. Briefly, renal sections were deparaffinized, rehydrated, subjected to antigen retrieval, and blocked. Subsequently, sections were stained with an anti-PCNA antibody (ab92552, Abcam, UK) followed by the corresponding secondary antibody (ab6721, Abcam, UK) to evaluate cell proliferation. Microvessel density (MVD) was quantified by counting the number of microvessels per high-power field, using an anti-CD31 antibody (ab182981, Abcam, UK) and the appropriate secondary antibody (ab6721, Abcam, UK). Moreover, cell apoptosis in kidney sections was assessed using a terminal transferase-mediated deoxyuridine triphosphate nick-end-labeling (TUNEL) assay, according to the manufacturer's instructions (ab206386, Abcam, UK).

For statistical analysis, three sections were prepared for each kidney sample, and 10 fields of view (200 × magnification) were randomly selected from each section. PCNA/TUNEL-positive cells (identified by dark-stained nuclei) were then counted using ImageJ software (Rasband, W.S., ImageJ, U. S. National Institutes of Health, USA). Two individual researchers analyzed the results separately, and the percentage of positive cells to the total number of cells was calculated.

5.13. Serum biochemical assessment

Renal function was evaluated by measuring serum urea nitrogen (BUN) and serum creatinine (Scr) levels. At days 1 and 7 post-reperfusion, blood samples from each group of rats were collected and centrifuged at 2000 rpm for 20 min to obtain the supernatants. The assays were conducted using an automated biochemical analyzer (Chemray 800, Rayto, China), employing BUN and Scr assay kits (S03036 and S03076, Rayto, China) as per the manufacturer's instructions.

Similarly, myocardial and hepatic functions were assessed using supernatants from rat blood samples. The evaluations were conducted with an automated biochemical analyzer (Chemray 800, Rayto, China), according to the manufacturer's instructions. For myocardial function assessment, creatine kinase (CK) and lactate dehydrogenase (LDH) assay kits (S03024 and S03034, Rayto, China) were utilized, while alanine aminotransferase (ALT) and aspartate aminotransferase (AST) assay kits (S03030 and S03040, Rayto, China) were employed to evaluate hepatic function.

To evaluate the coagulation function, prothrombin time (PT) and activated partial thromboplastin time (APTT) were examined. Briefly, blood samples were collected from the rats into tubes containing sodium citrate. These samples were then subjected to centrifugation at 3000 rpm for 15 min to obtain the plasma supernatant. The coagulation parameters were analyzed using an automated coagulation analyzer (RAC-1830, Rayto, China) with matched assay kits (R01002 and R01102, Rayto, China).

5.14. MiRNA sequencing of N-EVs

Total RNA from EVs and N-EVs was meticulously isolated utilizing the Trizol reagent (R401, Vazyme, China), strictly adhering to the manufacturer's protocols. RNA molecules in the range of 18–30 nt are enriched using polyacrylamide gel electrophoresis (PAGE). The subsequent miRNA sequencing assay was conducted by the established procedures provided by Illumina (USA), including library preparation and sequencing experiments. Specifically, the preparation of the small RNA sequencing libraries was accomplished using the TruSeq Small RNA Sample Prep Kits (Illumina, USA). Following the successful preparation of these libraries, they were subjected to high-throughput sequencing using the Illumina HiSeq 2500 platform (Illumina, USA), employing a single-ended read length of 1x50 base pairs.

5.15. Quantitative Real-time PCR

Following the manufacturer's protocol, miRNA was extracted using the MiPure Cell/Tissue miRNA Kit (RC201, Vazyme, China) and

subsequently reverse-transcribed into cDNA with the miRNA 1st Strand cDNA Synthesis Kit (MR101, Vazyme, China). Gene expression normalization was achieved using U6 (internal control) and cel-miR-39 (external control). Total RNA was isolated utilizing the VeZol Reagent (R411, Vazyme, China) and then reverse-transcribed into cDNA employing the HiScript II 1st Strand cDNA Synthesis Kit (R211, Vazyme, China), with GAPDH serving as the reference gene. RNA concentrations were quantified using a spectrophotometer (NanoDrop, Thermo Fisher, USA). Relative gene expression levels were determined through the comparative CT method ($2^{-\Delta\Delta Ct}$). The primer sequences employed in PCR analysis are detailed in Table S1.

5.16. Matrigel plug assay

Precooled growth factor-reduced Matrigel was mixed with PBS, N-EVs$^{Anta\text{-}NC}$, and N-EVs$^{Anta\text{-}miR-21-5p}$ in a volume ratio of 2:1, after which the mixture was subcutaneously injected into the dorsal region of nude mice. After 2 weeks, the Matrigel plugs were collected from each group. A hemoglobin assay kit (P0381S, Beyotime, China) was used according to the manufacturer's instructions to assess angiogenesis of Matrigel plugs in each group.

5.17. In vivo safety analysis

SD rats (6–8 weeks old) were intravenously injected with PBS, EVs, and N-EVs (400 μg per rat) once a week for 4 weeks. Blood samples were collected at certain time points to extract serum or plasma for relevant assays. Specifically, for coagulation analysis, blood was collected 2 h following the initial injection. On the final day of the experiment, prior to euthanasia, blood samples were obtained from each group to evaluate cardiac, hepatic, and renal functions. Additionally, major organs—including the heart, lungs, liver, spleen, and kidneys—were harvested from each group for HE staining to assess potential organ damage. The detailed experimental procedures were described in the previous sections.

5.18. Statistical analysis

Data analysis was performed utilizing GraphPad Prism software. All results are presented as mean ± standard deviation. Comparisons between two groups were conducted using two-tailed unpaired Student's t-tests, while comparisons among multiple groups were executed using one-way analysis of variance (ANOVA) with post hoc Tukey's tests. $P < 0.05$ (*) was considered statistically significant.

CRediT authorship contribution statement

Di Wu: Writing – review & editing, Writing – original draft, Validation, Investigation, Formal analysis, Conceptualization. **Wenjie Ma:** Validation, Software, Methodology, Investigation, Conceptualization. **Liucheng Wang:** Software, Resources, Methodology, Investigation, Formal analysis. **Chengcheng Long:** Resources, Project administration, Methodology. **Silin Chen:** Writing – review & editing, Investigation. **Jingyu Liu:** Visualization, Methodology, Formal analysis. **Yiguan Qian:** Software, Methodology. **Jun Zhao:** Software, Resources. **Changcheng Zhou:** Writing – review & editing, Supervision, Funding acquisition, Conceptualization. **Ruipeng Jia:** Writing – review & editing, Supervision, Funding acquisition, Conceptualization.

Ethics approval statement

The animal study protocol was approved by the Ethics Committee for the Use of Experimental Animals at Nanjing First Hospital, Nanjing Medical University.

Availability of data and materials

The datasets that support the findings of this study are available from the corresponding author upon reasonable request.

Funding

This research was funded by the National Natural Science Foundation of China (grant number 92049111, 82100802), Science and Technology Development Foundation of Nanjing Medical University (grant number NMUB20210193), the Open Research Fund of State Key Laboratory of Digital Medical Engineering(2024-M01), and Jiangsu Provincial Social Development Project (grant number BE2023661).

Declaration of competing interest

The authors declare that they have no known competing financial interests or personal relationships that could have appeared to influence the work reported in this paper.

Abbreviations

AKI	acute kidney injury
ALT	alanine aminotransferase
ANOVA	one-way analysis of variance
Anta-miR-21-5p	miRNA-21-5p antagomir
Anta-NC	miRNA antagomir negative control
APTT	activated partial thromboplastin time
AST	aspartate aminotransferase
BSA	bovine serum albumin
BUN	blood urea nitrogen
CK	creatine kinase
CKD	chronic kidney disease
ECs	endothelial cells
ECL	enhanced chemiluminescent
EPCs	endothelial progenitor cells
EVs	extracellular vesicles
GO	gene ontology
HE	hematoxylin and eosin
HRGECs	human renal glomerular endothelial cells
H/R	hypoxic/reoxygenated
IEM	immunogold-stained transmission electron microscopy
IRI	ischemia-reperfusion injury
KEGG	kyoto encyclopedia of genes and genomes
LDH	lactate dehydrogenase
miR-21-5p	miRNA-21-5p
MVD	microvessel density
NEs	neutrophils
N-EVs	neutrophils membrane-modified extracellular vesicles
NMVs	neutrophils membrane vesicles
NTA	nanoparticle tracking analysis
OD	optical density
PAGE	polyacrylamide gel electrophoresis
PBMCs	peripheral blood mononuclear cells
PBS	phosphate-buffered saline
PCNA	proliferating cell nuclear antigen
PFA	paraformaldehyde
PSGL-1	p-selectin glycoprotein ligand-1
PT	prothrombin time
RT	room temperature
Scr	serum creatinine
TEER	transendothelial electrical resistance
TEM	transmission electron microscope
TUNEL	terminal transferase-mediated deoxyuridine triphosphate nick-end-labeling
WB	western blotting

Appendix A. Supplementary data

Supplementary data to this article can be found online at https://doi.org/10.1016/j.mtbio.2025.101528.

Data availability

Data will be made available on request.

References

[1] M. Malek, M. Nematbakhsh, Renal ischemia/reperfusion injury; from pathophysiology to treatment, J. Ren. Inj. Prev. 4 (2) (2015) 20–27.
[2] A. Pefanis, F.L. Ierino, J.M. Murphy, P.J. Cowan, Regulated necrosis in kidney ischemia-reperfusion injury, Kidney Int. 96 (2) (2019) 291–301.
[3] C. Ronco, R. Bellomo, J.A. Kellum, Acute kidney injury, Lancet 394 (10212) (2019) 1949–1964.
[4] N. Jourde-Chiche, F. Fakhouri, L. Dou, et al., Endothelium structure and function in kidney health and disease, Nat. Rev. Nephrol. 15 (2) (2019).
[5] J.V. Bonventre, L. Yang, Cellular pathophysiology of ischemic acute kidney injury, J. Clin. Investig. 121 (11) (2011) 4210–4221.
[6] M.A. Kumar, S.K. Baba, H.Q. Sadida, et al., Extracellular vesicles as tools and targets in therapy for diseases, Signal Transduct. Targeted Ther. 9 (1) (2024) 27.
[7] E.D. Quiñones, M.-H. Wang, K.-T. Liu, et al., Extracellular vesicles from human adipose-derived stem cell spheroids: characterization and therapeutic implications in diabetic wound healing, Mater Today Bio 29 (2024) 101333.
[8] H. Peng, W. Ji, R. Zhao, et al., Exosome: a significant nano-scale drug delivery carrier, J. Mater. Chem. B 8 (34) (2020) 7591–7608.
[9] K. Chen, Y. Li, L. Xu, et al., Comprehensive insight into endothelial progenitor cell-derived extracellular vesicles as a promising candidate for disease treatment, Stem Cell Res. Ther. 13 (1) (2022) 238.
[10] Y. Zhang, H. Huang, W. Liu, et al., Endothelial progenitor cells-derived exosomal microRNA-21-5p alleviates sepsis-induced acute kidney injury by inhibiting RUNX1 expression, Cell Death Dis. 12 (4) (2021) 335.
[11] Z. He, H. Wang, L. Yue, Endothelial progenitor cells-secreted extracellular vesicles containing microRNA-93-5p confer protection against sepsis-induced acute kidney injury via the KDM6B/H3K27me3/TNF-α axis, Exp. Cell Res. 395 (2) (2020) 112173.
[12] F.-Y. Lee, C.-W. Luo, C.G. Wallace, et al., Direct implantations of erythropoietin and autologous EPCs in critical limb ischemia (CLI) area restored CLI area blood flow and rescued remote AMI-induced LV dysfunction, Biomed. Pharmacother. 118 (2019) 109296.
[13] T. Imai, Y. Takahashi, M. Nishikawa, et al., Macrophage-dependent clearance of systemically administered B16BL6-derived exosomes from the blood circulation in mice, J. Extracell. Vesicles 4 (2015) 26238.
[14] D. Chu, X. Dong, X. Shi, C. Zhang, Z. Wang, Neutrophil-based drug delivery systems, Adv. Mater. 30 (22) (2018) e1706245.
[15] W. Ma, D. Wu, C. Long, et al., Neutrophil-derived nanovesicles deliver IL-37 to mitigate renal ischemia-reperfusion injury via endothelial cell targeting, J. Contr. Release 370 (2024) 66–81.
[16] A. Hidalgo, A.J. Peired, M. Wild, D. Vestweber, P.S. Frenette, Complete identification of E-selectin ligands on neutrophils reveals distinct functions of PSGL-1, ESL-1, and CD44, Immunity 26 (4) (2007) 477–489.
[17] M. Phillipson, P. Kubes, The neutrophil in vascular inflammation, Nat. Med. 17 (11) (2011) 1381–1390.
[18] J. Gao, D. Chu, Z. Wang, Cell membrane-formed nanovesicles for disease-targeted delivery, J. Contr. Release 224 (2016) 208–216.
[19] J. Gao, S. Wang, Z. Wang, High yield, scalable and remotely drug-loaded neutrophil-derived extracellular vesicles (EVs) for anti-inflammation therapy, Biomaterials 135 (2017) 62–73.
[20] T. Rogers, R.J. DeBerardinis, Metabolic plasticity of neutrophils: relevance to pathogen responses and cancer, Trends Cancer 7 (8) (2021) 700–713.
[21] Z. Xing, C. Zhao, H. Liu, Y. Fan, Endothelial progenitor cell-derived extracellular vesicles: a novel candidate for regenerative medicine and disease treatment, Adv. Healthcare Mater. 9 (12) (2020) e2000255.
[22] J.R. Albe, D.A. Boyles, A.W. Walters, et al., Neutrophil and macrophage influx into the central nervous system are inflammatory components of lethal Rift Valley fever encephalitis in rats, PLoS Pathog. 15 (6) (2019) e1007833.
[23] A.A. Salybekov, S. Kobayashi, T. Asahara, Characterization of endothelial progenitor cell: past, present, and future, Int. J. Mol. Sci. 23 (14) (2022).
[24] M. Mathieu, N. Névo, M. Jouve, et al., Specificities of exosome versus small ectosome secretion revealed by live intracellular tracking of CD63 and CD9, Nat. Commun. 12 (1) (2021) 4389.
[25] D.P. Basile, The endothelial cell in ischemic acute kidney injury: implications for acute and chronic function, Kidney Int. 72 (2) (2007) 151–156.
[26] J.V. Bonventre, A. Zuk, Ischemic acute renal failure: an inflammatory disease? Kidney Int. 66 (2) (2004) 480–485.
[27] Q. Zhang, C. Hu, J. Feng, et al., Anti-inflammatory mechanisms of neutrophil membrane-coated nanoparticles without drug loading, J. Contr. Release 369 (2024) 12–24.
[28] H. Hu, B. Wang, C. Jiang, R. Li, J. Zhao, Endothelial progenitor cell-derived exosomes facilitate vascular endothelial cell repair through shuttling miR-21-5p to modulate Thrombospondin-1 expression, Clin. Sci. 133 (14) (2019) 1629–1644.
[29] S. Terriaca, E. Fiorelli, M.G. Scioli, et al., Endothelial progenitor cell-derived extracellular vesicles: potential therapeutic application in tissue repair and regeneration, Int. J. Mol. Sci. 22 (12) (2021).
[30] N. Barrionuevo, S. Gatica, P. Olivares, C. Cabello-Verrugio, F. Simon, Endothelial cells exhibit two waves of P-selectin surface aggregation under endotoxic and oxidative conditions, Protein J. 38 (6) (2019) 667–674.
[31] A. Zarbock, K. Ley, R.P. McEver, A. Hidalgo, Leukocyte ligands for endothelial selectins: specialized glycoconjugates that mediate rolling and signaling under flow, Blood 118 (26) (2011) 6743–6751.
[32] J. Chen, Y. Song, Q. Wang, et al., Targeted neutrophil-mimetic liposomes promote cardiac repair by adsorbing proinflammatory cytokines and regulating the immune microenvironment, J. Nanobiotechnol. 20 (1) (2022) 218.
[33] D. Han, F. Wang, Z. Qiao, et al., Neutrophil membrane-camouflaged nanoparticles alleviate inflammation and promote angiogenesis in ischemic myocardial injury, Bioact. Mater. 23 (2023) 369–382.
[34] M. Tkach, C. Théry, Communication by extracellular vesicles: where we are and where we need to go, Cell 164 (6) (2016) 1226–1232.
[35] L. Qiao, S. Hu, S. Liu, et al., microRNA-21-5p dysregulation in exosomes derived from heart failure patients impairs regenerative potential, J. Clin. Investig. 129 (6) (2019) 2237–2250.
[36] J. Liu, Q. Dou, C. Zhou, et al., Low-energy shock wave pretreatment recruit circulating endothelial progenitor cells to attenuate renal ischaemia reperfusion injury, J. Cell Mol. Med. 24 (18) (2020) 10589–10603.
[37] Q. Zhang, D. Dehaini, Y. Zhang, et al., Neutrophil membrane-coated nanoparticles inhibit synovial inflammation and alleviate joint damage in inflammatory arthritis, Nat. Nanotechnol. 13 (12) (2018) 1182–1190.
[38] Y. He, R. Li, H. Li, et al., Erythroliposomes: integrated hybrid nanovesicles composed of erythrocyte membranes and artificial lipid membranes for pore-forming toxin clearance, ACS Nano 13 (4) (2019) 4148–4159.
[39] S.A. Melo, L.B. Luecke, C. Kahlert, et al., Glypican-1 identifies cancer exosomes and detects early pancreatic cancer, Nature 523 (7559) (2015) 177–182.
[40] C. Théry, S. Amigorena, G. Raposo, A. Clayton, Isolation and characterization of exosomes from cell culture supernatants and biological fluids, Curr. Protoc. Cell Biol. (2006). Chapter 3:Unit 3.22.
[41] C. Zhou, L. Zhou, J. Liu, et al., Kidney extracellular matrix hydrogel enhances therapeutic potential of adipose-derived mesenchymal stem cells for renal ischemia reperfusion injury, Acta Biomater. 115 (2020) 250–263.